Solar Physics (2024) 299:129
https://doi.org/10.1007/s11207-024-02373-0

RESEARCH

Mysteries of the 17 May 2012 Solar Event Responsible for GLE71. I. CME Development and the Role of Disturbances Excited by Eruptions

V.V. Grechnev[1] · V.I. Kiselev[1] · A.M. Uralov[1] · N.S. Meshalkina[1] · K.A. Firoz[2] · A.L. Lysenko[3]

Received: 31 May 2024 / Accepted: 9 September 2024

Abstract

The SOL2012-05-17 event is remarkable in that it caused one of two ground-level enhancements (GLE71) in Solar Cycle 24. Despite the efforts spent studying this solar event, some aspects of it remain unclear. This relates to the development of a coronal mass ejection (CME), the history of the shock wave, and the flare. Our measurements reveal the following chain of phenomena. Two successive eruptions occurred within a few minutes. The rate of change of the reconnected magnetic flux shows a series of increases corresponding to the acceleration or deceleration of the erupting structures. The temporal profile of the magnetic-flux change rate is similar to the hard X-ray burst. Each eruption excited a disturbance that, propagating outward, accelerated all structures above it. This led to complex kinematic characteristics of the erupting structures that eventually formed a self-similarly expanding CME. The two disturbances became piston shocks and merged into a single, stronger shock. There are indications of transformation of the piston shock into a bow shock, but this occurs at distances exceeding ten solar radii. Components of the described picture were observed in a number of events and can serve as a guide for studies of eruptive flares.

✉ V.V. Grechnev
grechnev@iszf.irk.ru

V.I. Kiselev
valentin_kiselev@iszf.irk.ru

A.M. Uralov
uralov@iszf.irk.ru

N.S. Meshalkina
nata@iszf.irk.ru

K.A. Firoz
kaziabulfiroz@pmo.ac.cn

A.L. Lysenko
alexandra.lysenko@mail.ioffe.ru

1 Institute of Solar-Terrestrial Physics SB RAS, Lermontov St. 126A, Irkutsk 664033, Russia

2 Key Laboratory of Dark Matter and Space Astronomy, Purple Mountain Observatory, Chinese Academy of Sciences, Nanjing, 210023, People's Republic of China

3 Ioffe Institute, Polytekhnicheskaya 26, St. Petersburg, 194021, Russia

Published online: 20 September 2024

Keywords Coronal mass ejections · Flares · Magnetic reconnection · Radio bursts · Waves

1. Introduction

Ground-level enhancements of the cosmic-ray intensity (GLEs) occur when secondary particles produced by collisions of near-relativistic solar protons with nuclei of the Earth's atmosphere reach the ground, where they are detected by neutron monitors. Over 81 years of observations from 1942 to 2023, only 73 such events were recorded (e.g., Miroshnichenko, Vashenyuk, and Pérez-Peraza 2013; Anastasiadis et al. 2019). Most likely, GLEs represent the highest-energy subset of solar energetic particle (SEP) events rather than a separate class of events (e.g., Moraal and McCracken 2012; Bruno et al. 2018). Obviously, GLE events attract special attention.

The origin of accelerated protons and heavier ions that are part of SEPs, in general, and high-energy protons responsible for GLEs in particular, is a long-standing unresolved issue. Two possible accelerators of heavy charged particles are being considered. One is related to flare processes caused by magnetic reconnection in an active region (e.g., Klein and Trottet 2001; Kallenrode 2003; Aschwanden 2012). Another probable accelerator of protons is a shock wave associated with a fast coronal mass ejection (CME) (e.g., Cliver, Kahler, and Reames 2004; Gopalswamy et al. 2012; Reames 2013). Some studies (e.g., Cane, Richardson, and von Rosenvinge 2010; Anastasiadis et al. 2019) have shown that, at least for some events, acceleration both by flare processes and CME-associated shock wave appear to have contributed to the same near-Earth proton enhancement. Efforts to identify the possible contribution of each of these sources have not yet met with recognized success, so that when considering high-energy solar protons, one has to rely largely on indirect indications based on hypotheses that have not been exhaustively verified.

The 17 May 2012 solar event was the source of the seventy-first GLE (e.g., Gopalswamy et al. 2013b), the first of only two GLEs to occur in Solar Cycle 24. Studies of this event and its consequences seem to be favored by the availability of detailed observations of several instruments from different vantage points in the heliosphere. This made it possible to reconstruct the shapes of the CME and the shock front ahead of it in three dimensions. The spectrum of the SEP event at high energies was measured with unprecedented detail and accuracy (e.g., Whitman et al. 2017; Bruno et al. 2018). The availability of a detailed SEP spectrum, multi-spacecraft in-situ measurements, progress in understanding the proton propagation in the interplanetary space, and the development of various models have provided the basis for a number of studies of the SEP and GLE event.

Gopalswamy et al. (2013b) analyzed the CME kinematics using the *Graduated Cylindrical Shell* model (GCS model: Thernisien, Vourlidas, and Howard 2009; Thernisien 2011), studied the relationship of the CME with the Type-II burst and SEP acceleration, and advocated the shock-related origin of the SEP and GLE protons. A similar conclusion was drawn by Li et al. (2013), who studied electron acceleration in relation to the Type-III burst as well as proton acceleration in relation to the CME shock. Shen et al. (2013) and Rouillard et al. (2016) basically shared the same point of view. Firoz et al. (2014) studied SEP acceleration in relation to the CME-associated shock evolution and found indications of both flare-acceleration and shock-acceleration of GLE particles. Pérez-Peraza et al. (2018) compared the modeled and observed spectra of the prompt and delayed GLE components and concluded, unlike most of the listed studies, that the pure shock acceleration does not play a major role in accelerating particles to GLE energies.

Several studies addressed particle transport in interplanetary space, using advanced modeling techniques and comparing the results with observations. Battarbee et al. (2018) modeled the SEP event and compared their results with multi-spacecraft observations. Dalla et al. (2020) performed three-dimensional (3D) modeling of the transport of GLE-energy solar protons to assess the transport effects in the interplanetary space. Comparison of the simulation results with near-Earth observations on 17 May 2012 allowed the authors to estimate the size of the injection region, a mean free path, and injection spectrum. Palmerio et al. (2021) studied the interplanetary context at the time of the 17 May 2012 eruption and, using observations of the SEP event at eight locations in the inner heliosphere, demonstrated that the presence of a preceding CME, which was launched several days before, facilitated particle transport (Rouillard et al. 2016 came to a similar conclusion).

The 17 May 2012 solar event was associated with an M5.1 flare in active region 11476 that started at 01:25, peaked at 01:47, and ended at 02:14 according to GOES observations. The flare location was reported to be N11 W76. The event led to a fast CME with an average speed of 1580 km s^{-1} according to the online CME catalog of the *Coordinated Data Analysis Workshop* (CDAW) (cdaw.gsfc.nasa.gov/CME_list/: Yashiro et al. 2004). A Type-II burst was observed by several spectrographs, starting at 01:32 from meters to hectometers.

Notable are the studies of this event by Shen et al. (2013) and by Rouillard et al. (2016), both of which employed 3D reconstructions, have contributed to knowledge of this event and provided suggestions for possible causes of the large proton enhancement and GLE. Both studies assumed excitation of a bow shock ahead of the fast CME.

Shen et al. (2013) reconstructed a pre-eruption twisted flux-rope progenitor, studied the initiation stage of the eruptive event, and revealed subsequent erupting structures. Based on the same GCS model as Gopalswamy et al. (2013b) used, the authors proposed that this event produced two CMEs that developed one after another within two minutes. According to the authors, each of the two CMEs drove a shock and the entire event was consistent with the twin-CME scenario proposed by Li et al. (2012). In this scenario, a combined action of the first, slower, narrower CME, and the second, faster, wider CME that expands shortly after the first, results in a more efficient particle acceleration than in the case of a single CME-driven shock. Although the idea of Shen et al. (2013) seems promising, it is difficult to understand what happened in the event and how the CME(s) developed unless the movements of the erupting structures and the expansion of structural components of the CME are measured.

Rouillard et al. (2016) developed and applied to the 17 May 2012 event an advanced 3D technique to reconstruct the expansion of the shock forming in the corona. The authors derived the 3D velocity vector and the distribution of Mach numbers of the entire front as a function of time that corresponded to the bow-shock regime. The authors also studied the magnetic connectivity between the region of the appropriate Mach number they found and the near-Earth environment, presented the event-integrated proton-fluence spectrum vs. rigidity, corresponding to energies from a few MeV to 1.4 GeV, and discussed the solar particle release time estimated from the velocity-dispersion analysis.

While this extensive study appears impressive, some questions remain. First, it is unclear whether there were actually two CMEs with two shock waves, as Shen et al. (2013) proposed, or just one. Second, the bow-shock excitation from the very beginning is difficult to reconcile with the conclusions drawn by us, as well as by other authors, about the more complex shock-wave history, from piston shock to blast wave and then to the bow shock if the CME is fast, or its decay if the CME is slow or absent (e.g., Bain et al. 2012; Zimovets et al. 2012; Grechnev, Kiselev, and Uralov 2022). Third, examples of events where protons are accelerated exclusively by shock waves in the obvious absence of flare-accelerated particles, when higher-energy protons arrive at the Earth orbit later than lower-energy protons,

show that the velocity-dispersion analysis may not be applicable in such cases (Grechnev and Kuzmenko 2020). These challenges indicate that the shock-wave history in this event is not well understood.

Little is known about the flare in this event. In particular, this is due to the fact that the *Reuven Ramaty High-Energy Solar Spectroscopic Imager* (RHESSI: Lin et al. 2002) missed most of the flare and observed only its last part, while *Fermi* missed the flare altogether. Firoz et al. (2017) studied the late-phase thermal emission of this flare using RHESSI data. Grechnev et al. (2013, 2015) found that the microwave burst in this flare was atypically moderate in comparison with other large proton events. We are not aware of any information about the reconnected magnetic flux.

Thus, neither of the possible sources of accelerated protons in this event, the flare and the shock wave, has been sufficiently explored and both need greater understanding. As mentioned, this requires measurements of the movements of erupting structures and the expansion of structural components of the CME. The results of these measurements make it possible to establish the sequence of phenomena and identify causal relationships. These will help to understand the CME development that still remains unclear (e.g., Howard, Vourlidas, and Stenborg 2023). Finally, an important problem is to identify the contributions of flare processes and shock waves to the acceleration of solar protons reaching the Earth orbit. The key to solving this problem has not yet been found. Elucidation of the actual development of the CME, shock wave, and flare promises insight into particle acceleration beyond assumption-based considerations.

Our two companion articles aim to shed light on these issues. This article (Article I) addresses eruptions, CME development, shock-wave history, and the relationship between eruptions, flare, and reconnection processes. Article II (in preparation) considers particularity of the flare configuration, the atypical microwave burst, and its relationship with reconnection rate.

This article is organized as follows. Section 2 introduces the event. Section 3 addresses eruptions and CME. Section 4 discusses shock-wave manifestations in coronagraph images and radio emission. Section 5 considers manifestations of reconnection and its relationship with other phenomena. Section 6 discusses the results and provides concluding remarks that may benefit future studies.

Because of the complexity of this event, instead of presenting a chronological order of phenomena, we consider observations following the logic of identifying causal relationships between these phenomena and revealing corresponding observational indications. This caused some repetitions in our figures and considerations of the event.

2. Brief Overview of the Event

The 17 May 2012 eruptive-flare event was observed by several instruments from different vantage points. We analyze the eruptions using mainly the images obtained by the *Atmospheric Imaging Assembly* (AIA: Lemen et al. 2012) on board the *Solar Dynamics Observatory* (SDO: Pesnell, Thompson, and Chamberlin 2012), which observed the event from the Earth's direction. Additional information in a wider field of view is provided by 174 Å images from the *Sun Watcher using Active Pixel system detector and image processing* imager (SWAP: Berghmans et al. 2006) on board the *Project for On-Board Autonomy* (PROBA2: Santandrea et al. 2013) micro-satellite. For the analysis of the CME we use the images from the *Large Angle Spectroscopic Coronagraph* (LASCO: Brueckner et al. 1995) on board the *Solar and Heliospheric Observatory* (SOHO: Domingo, Fleck, and Poland 1995).

The flare site was also observed by the *Sun Earth Connection Coronal and Heliospheric Investigation* instrument suite (SECCHI: Howard et al. 2008) on the Ahead spacecraft of the *Solar-Terrestrial Relations Observatory* (STEREO: Kaiser et al. 2008) that was located 114.8° westward from the Earth. We use the images produced by the *Extreme Ultraviolet Imager* (EUVI: Wuelser et al. 2004) on board STEREO-A and by the inner coronagraphs COR1 (Howard et al. 2008) on board STEREO-A and STEREO-B (the latter was located 117.6° eastward from the Earth).

Figure 1 presents the development of the flare ribbons observed in 1600 Å by SDO/AIA (left column) and in 171 Å by STEREO-A/EUVI (right column). The chains of coronal brightenings visible in 171 Å trace the ribbons beneath them. A comparison of the images obtained by the two telescopes from different vantage points reveals at least two pairs of ribbons, some of which are indicated by arrows in Figure 1d. This suggests that more than one eruption occurred there. The yellow-dotted arc in Figure 1d denotes the southwestern boundary of the post-eruption arcade that subsequently formed there, i.e., the ends of the ribbons. The SDO/AIA and STEREO-A/EUVI image pairs indicate that the southwestern extension of the flaring structure looks more like a prominence that activated during the event.

Images from STEREO-A/EUVI, which observed the flare site further from the limb than it was visible from the Earth's direction, make it possible to refine its coordinates, which varied in different studies. Referring to the heliographic grid in Figure 1h that corresponds to the view from the Earth's direction, the position of the main flare site was N06 W78.

Figure 2 presents the CME bubble in reduced-resolution running-difference SDO/AIA 193 Å images. The following circumstances can be noted:

i) The structure labeled 'F' was the outermost structure of the CME bubble and therefore likely subsequently became the CME-body front.
ii) The outermost structure of the CME bubble expanded later and more slowly than the structures inside it. Therefore, these internal structures were most likely responsible for the expansion of the entire CME.
iii) A thick bright halo on top of the CME-bubble front indicates a compressed layer of plasma pile-up, suggesting the association of the front with a separatrix surface. Similar halos appear ahead of internal CME-bubble structures. The work of displacing magnetoplasma from the volume it previously occupied is performed due to the energy of the driver of the CME expansion. This circumstance also determines the kinematic characteristics of the disturbances generated by this driver.

The internal structures of the CME bubble are shown in the next figure. Figure 3 presents moving features revealed from SDO/AIA images in different channels, in agreement with the findings of Shen et al. (2013). The background in this figure are AIA images obtained in the 94 Å channel, which shows a relatively hot plasma (about 6 MK) and suffers little from overexposure distortions. The outer edges of these moving features are outlined with arcs of different colors, which we use henceforth for these same features, their likely successors, and corresponding kinematic characteristics.

Figure 3a shows a complex structure that looks like a bundle of heated loops. The top of this structure, labeled 1, started expanding a little earlier than the brighter feature 2. It is not excluded that one of features 1 and 2 could be located behind the other at a considerable distance. In Figure 3b, feature 2 displaced forward and a blob-like feature 3 started to move nearly along the limb. A long loop-like structure 4, outlined with the orange arc, possibly part of a prominence (see Figure 1d), became visible. In Figure 3c, feature 3 approached structure 4 and then, after their apparent collision, the cross-section of structure 4 started to expand.

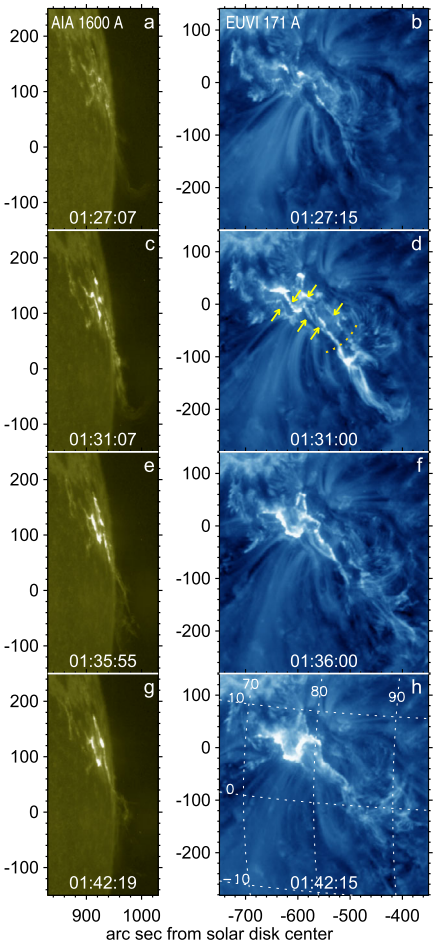

Figure 1 Development of the eruptive flare as observed by SDO/AIA in 1600 Å (*left*) and by STEREO-A/EUVI in 171 Å (*right*). *Yellow arrows* in panel **d** indicate flare ribbons. The *yellow-dotted arc* denotes the southwestern boundary of the post-eruption arcade that appeared later there. The *heliographic grid* in panel **h** corresponds to the view from the Earth's direction.

These eruptions gave rise to a fast CME. In the next section we consider its structural components and estimate their speeds. This will make it possible to identify their predecessors and then reconstruct their kinematic characteristics.

3. CME and Eruptions

3.1. Structural Components of the CME and Their Expansion

Figure 4 presents six images of the CME that were produced by the LASCO-C2 and -C3 coronagraphs. To reveal the structure of the expanding CME, no image subtraction was used, and the contribution of static coronal structures was reduced by dividing each image by a fixed pre-event image (separately for C2 and C3). To better show the structure of the CME and its possible changes, the fields of view of the images were progressively enlarged so that the apparent size of the CME remained unchanged (see also the CME.mpg movie in the Electronic Supplementary Material). As the figure and the movie show, the expansion of the CME in this temporal interval was self-similar. The CME structure included three distinct

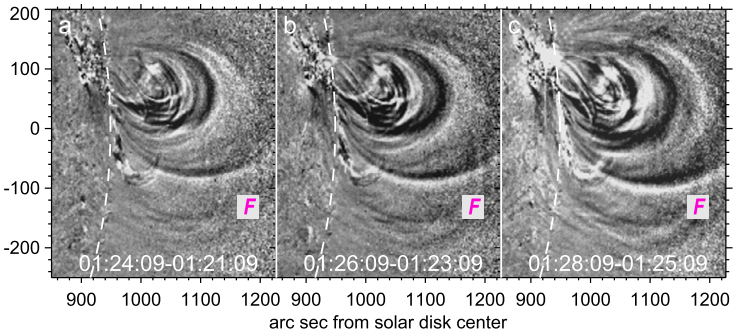

Figure 2 Appearance of the CME bubble in SDO/AIA 193 Å running-difference images. The *white-dashed arc* denotes solar limb. The outermost structure of the CME bubble is labeled *F*.

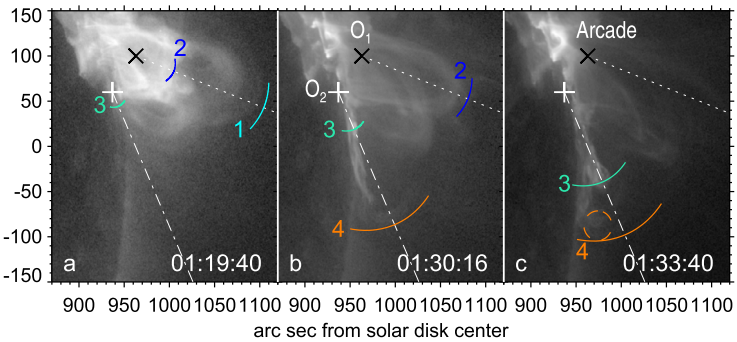

Figure 3 Moving features observed in SDO/AIA 94 Å images. The *color arcs* outline the outermost edges of the moving features. The *orange-dashed circle* outlines the visible outer boundary of the expanding loop-like structure. The *broken lines* correspond to the directions of movements along which the measurements discussed below were carried out from the origins marked with different *crosses* and denoted O_1 and O_2.

components, i.e., front (F), 1, and 2. These three components are outlined with colored arcs; their plane-of-sky speeds of 1600, 1050, and 980 km s^{-1}, respectively, were constant for more than two hours. The accuracy of our speed estimation is about ±5%. The speeds of the CME components are almost linearly related to their distances to the virtual expansion center, i.e., the speed ratio of 1600:1050:980 = 1.63:1.07:1 is close to the distance ratio of 1.64:1.09:1. This is a sign that in the interval of self-similar expansion, the magnetoplasma ejection retains its mass inside the volume enclosed by the front F (Uralov, Grechnev, and Hudson 2005).

The outermost CME component F is clearly defined and there are no CME-body magnetoplasma structures such as frontal loops or flux-rope components ahead of it. Our estimate of its speed is close to the average speed of the fastest feature of 1580 km s^{-1}, estimated in the online CDAW CME catalog (Yashiro et al. 2004: cdaw.gsfc.nasa.gov/CME_list/) in a close temporal interval. These facts allow identifying the CME front in Figure 4 with the outermost structure of the developing CME bubble in Figure 2, in agreement with item i in Section 2.

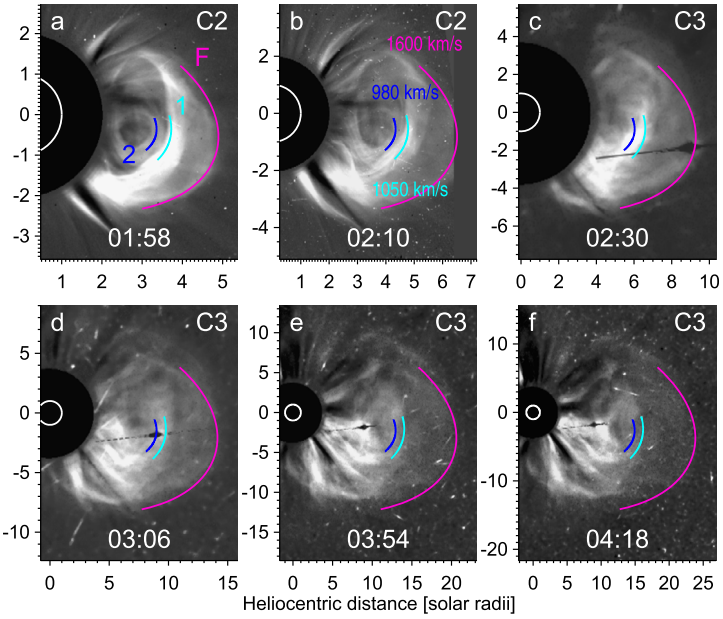

Figure 4 Distinct structural components of the CME in non-subtracted SOHO/LASCO-C2 and -C3 images. The *color arcs* outlining the CME components denoted *F*, *1*, and *2* correspond to constant speeds indicated in panel **b**. The fields of view of the images were progressively scaled to keep the visible size of the CME constant. The black disk with a long blooming streak in panels **c**–**f** is a trace of the image of Jupiter on the under-cleaned base LASCO image.

3.2. Two Main Eruptions

In this section, we first measure the movements of two erupting features 1 and 2 outlined in Figure 3a. For the measurements, we use two representations of running-difference AIA 193 Å images. The first representation is a sequence of images in which the leading edge of the feature of interest is detectable; we outline it with an arc of radius, which we optimize. The second representation is a one-dimensional spatial profile, each column of which is calculated as the sum across a relatively narrow strip of the given image along the measurement direction (e.g., Grechnev et al. 2014a). This representation is similar to well-known stack plots, providing a higher signal-to-noise ratio.

The shape of the acceleration pulse does not matter because of double integration. What is important is the time of its centroid (we also call it peak time), area, and duration. We use combinations of Gaussian-shaped acceleration pulses and manually optimize their parameters to fit the results of their double integration to the movements of the erupting features (e.g., Grechnev et al. 2011, 2019, 2022).

Figure 5 presents the movements of erupting features 1 and 2 along with their fit according to the measurements, Figure 6 presents their one-dimensional profile, and Figure 7 presents the kinematic plots. The AIA94_eruptions.mpg movie in the Electronic Supplementary Material shows the erupting features in more detail. The best visibility of erupting feature 2 and sufficient observation time ensured the greatest accuracy of its measurements. We estimate for its main acceleration pulse the peak time of 01:30:25 $\pm$10 s, the duration of 270 s $\pm$5%, and the final speed of 980 km s^{-1} $\pm$ 3%. The acceleration stage of this erupting feature was almost entirely within the field of view of AIA and its final speed coincides with

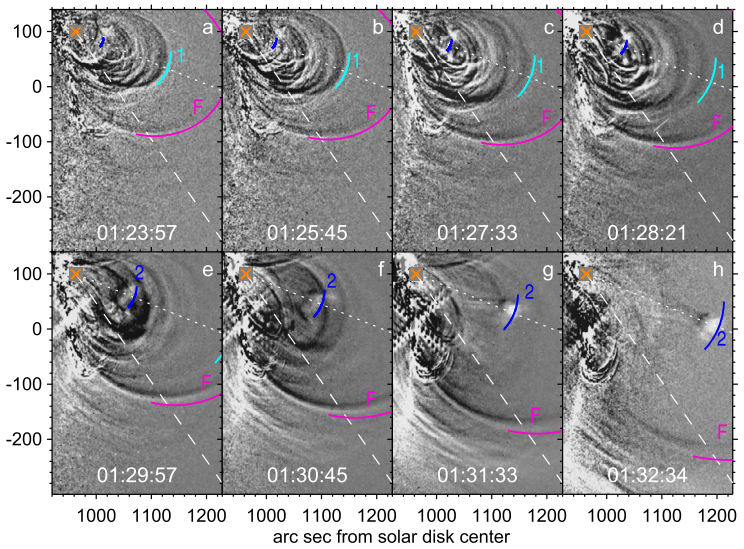

Figure 5 Erupting features 1 and 2 in SDO/AIA 193 Å running-difference images. The *cyan* and *blue arcs* outline their leading edges and the *magenta arc* outlines the CME-bubble front according to the kinematic plots in Figure 7. The *orange slanted cross* corresponds to origin O_1 denoted in Figure 3. The *dotted line* (same as in Figure 3) corresponds to the direction of motion of the main erupting features. The *dashed line* indicates the direction in which the spatial profiles of the CME-bubble front were measured.

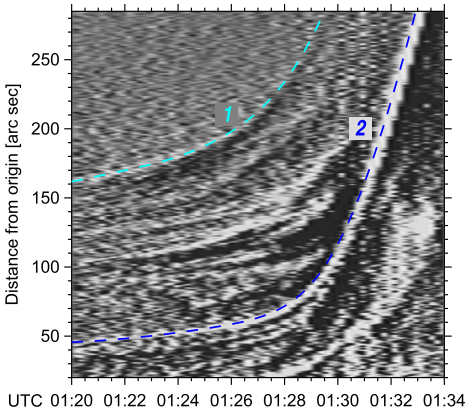

Figure 6 One-dimensional spatial profiles of erupting features *1* and *2* measured from origin O_1 in the direction indicated by the dotted line in Figures 3 and 5. The *cyan* and *blue dashed curves* outline the traces in the profiles according to the kinematic plots presented in Figure 7.

the speed of the CME structural component 2. This allows us to identify them with each other.

A slight acceleration of erupting feature 1 around 01:24 is noticeable only from the initial slope of its profile in Figure 6, and it should be attributed to the initiation stage in accordance with its speed of 108 km s^{-1} at 01:25 and 210 km s^{-1} at 01:27. Only part of its acceleration stage can be measured until 01:29:30, when its speed reached 500 km s^{-1}. On the other hand, the fact that feature 1 was located between the CME-bubble front and feature 2, as well as the structural component 1 of the CME between its front and component 2, indicates their

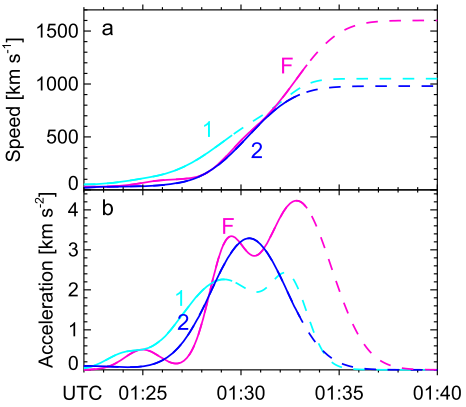

Figure 7 Speed–time (**a**) and acceleration–time (**b**) plots measured for the leading edges of erupting features *1* and *2* and the CME-bubble front *F*. The *solid* parts of the curves correspond to the intervals in which the measured features were within the field of view of AIA, and the *dashed* parts represent their presumable continuations to match the movements and the final speeds of these features as structural components of the CME in LASCO images.

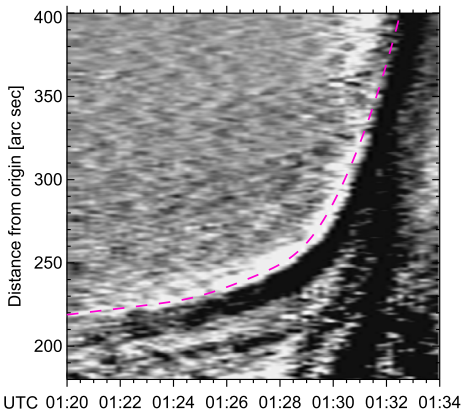

Figure 8 One-dimensional spatial profiles of the CME-bubble front measured from origin O_1 in the direction indicated by the dashed line in Figure 5. The *magenta-dashed curve* outlines the traces in the profiles according to the kinematic plot presented in Figure 7.

correspondence to each other. There must have been an additional acceleration of feature 1 later, which will be discussed in Section 3.3.

Finally, we measure the movement of the outermost front structure. From the very beginning, its top was located outside the field of view of AIA. Therefore, we measure the movement of its southern flank along the direction indicated by the dashed line in Figure 5, where its outer edge is outlined with the magenta arc. Figure 8 shows the one-dimensional profile. Figure 7 shows the kinematic plots that relate to the top of the front in the direction denoted with the dotted line in Figure 5 and corresponding to the measured movement of the southern flank.

The first acceleration pulse of the front is reliably measured in the field of view of AIA. The presence of the second acceleration pulse is also certain; without it, the outlining arc subsequently begins to noticeably lag behind the flank. Our measurements of the flank movement are also limited by the field of view of AIA and are not possible after 01:33. Because of this limitation, there is an increased uncertainty in the peak time and duration of the second acceleration pulse. However, with a known final speed of the CME-bubble front of 1600 km s^{-1}, the full temporal profile of its acceleration in Figure 7 is determined more or less definitely. The question arises what were the reasons for these two pulses of its acceleration. Likewise, the reason for the second acceleration pulse of erupting feature 1 is unclear.

To find answers to these questions, recall item ii in Section 2, indicating that the internal structures of the CME bubble were responsible for its expansion.

The results of our plane-of-the-sky measurements may be somewhat lower than in 3D space. Comparing the accelerations in Figure 7b directly measured in the AIA field of view with the CME acceleration of 1.77 $\mathrm{km\,s^{-2}}$ estimated by Gopalswamy et al. (2013b) using the GCS model shows the accuracy of the latter to be around a factor of two.

3.3. Unclear Additional Acceleration Episodes

If a magnetoplasma structure expands, then this causes the magnetic fields above it to also expand. In the simplest case of a weak linear disturbance, the speed of its transmission from the source to the outside is the fast-mode speed in the environment. Based on this simple consideration, it can be assumed that the disturbance produced by each eruption propagated outward and accelerated all overlying coronal structures. More specifically, i) the expansion of erupting feature 1 caused the first acceleration of the front, and ii) the expansion of erupting feature 2 caused an additional acceleration of erupting feature 1 and then the second acceleration of the front. Qualitatively, this assumption seems consistent with observations, but for a quantitative description the situation is more complex.

The acceleration pulses of eruptive features 1 and 2 measured in the AIA field of view exceeded 2 and 3 $\mathrm{km\,s^{-2}}$, i.e., more than 7 and 11 times the solar gravity acceleration, respectively. Such violent movements of magnetoplasma structures should certainly lead to strong disturbances in the surrounding corona. The propagation speeds of these disturbances are determined by the fast-mode speed in the environment and the piston speed (see Uralov, Grechnev, and Ivanukin 2019 for details). Bearing in mind item iii in Section 2, we describe the propagation of these disturbances using the power-law patterns that we previously applied to piston shocks (e.g., Grechnev et al. 2008, 2011; Grechnev, Kochanov, and Uralov 2023).

There are differences between this situation and the conditions to which the description mentioned applies. The smooth shapes of the acceleration pulses (i.e., their finite durations) show that the shock discontinuity has not yet been formed in the region under consideration. Therefore, instead of a localized shock front, we are dealing here with an extended zone of the disturbance, which has the form of a simple wave (e.g., Vršnak and Cliver 2008). The distance–time trajectory describing the piston-shock propagation here has the meaning of a characteristic corresponding to the steepest zone of the disturbance, while the actual wave packets are grouped into a band around this trajectory.

In addition, the model assumes that the piston shock is excited by a point source, while its onset corresponds to the maximum acceleration of the piston. To bring the idealized model closer to the situation under consideration, the onset time of the disturbance, which was actually excited by an extended source at the moment of its maximum acceleration, should be extrapolated to the location of the virtual point source (see Grechnev and Kuzmenko 2020 for an example).

We calculate the distance–time wave trajectory $x(t)$ using a power-law coronal-density model $n(x) = n_0(x/h_0)^{-\delta}$ with $[x]$ being the distance from the wave origin, $[n_0]$ the density at a distance $h_0 = 100$ Mm (close to the coronal scale height), and $[\delta]$ the density-falloff exponent (typically between 2.5 and 2.9). Then, the trajectory is $x(t) = x_1[(t - t_0)/(t_1 - t_0)]^{2/(5-\delta)}$, where $[x_1]$ is the distance from the origin to a wave front observed at time $[t_1]$ (Grechnev et al. 2008, 2011).

Applying this technique to our event, we adjusted the parameters of the trajectory of the first wave so that it started at point O_1, passed through feature 1 near the maximum of its

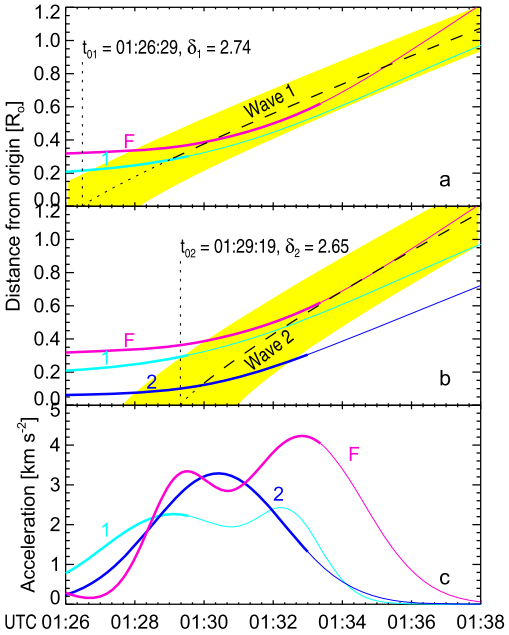

Figure 9 Kinematic plots of erupting features *1* and *2* and the CME-bubble front *F* along with the two presumable waves. **a**) Distance–time plots of the front and feature 1 (*solid curves*) along with wave 1 excited by feature 1. **b**) Distance–time plots of the front and features 1 and 2 (*solid curves*) along with wave 2 excited by feature 2. The *broken curves* in panels **a** and **b** represent the characteristic trajectories of the waves. Their *dotted portions* correspond to the extrapolations of the wave onset times to the locations of the virtual point sources. The *yellow shadings* schematically indicate the zones of influence of the waves. The horizontal widths of the yellow bands are close to the half-height widths of the acceleration pulses in panel **c**. **c**) Acceleration–time plots. The *thick* parts of the curves correspond to the intervals in which the measured features were observed, and the *thin* parts represent their presumable continuations. All plots relate to the direction indicated with the *dotted line* from origin O_1 denoted in Figures 3 and 5.

acceleration, and then passed through the front near the maximum of its acceleration. This was achieved with a virtual wave onset time $t_{01} = 01{:}26{:}29$ and $\delta_1 = 2.74$. Similarly, by setting the onset of the second wave at the same point O_1, its passage through feature 2 near the maximum of its acceleration and then through feature 1 near the maximum of its acceleration was achieved with $t_{02} = 01{:}29{:}19$ and $\delta_2 = 2.65$. Figures 9a and 9b demonstrate these results for the two first waves separately. For comparison, Figure 9c shows the acceleration–time plots. Bearing in mind that the curves refer to the leading edges of the measured features, we note that the second acceleration pulse of the front more or less corresponds to the passage of the second wave.

The yellow-shaded bands in Figures 9a and 9b represent the wave-influence zones only schematically. Due to the propagation of the disturbance into the regions of lower fast-mode speed, its profile should steepen that corresponds to a narrowing of the yellow band. When the shock discontinuity is formed, the band becomes a line.

The correspondence of the movements of erupting structures to the passage of the two waves through them is even better seen from Figure 10 and the AIA193_diff_waves.mpg movie in the Electronic Supplementary Material. Being similar to Figure 5, Figure 10 also shows the development of the two disturbances and their influence on the expansion of the erupting structures that is presented in more detail. The yellow-solid elliptic arcs represent

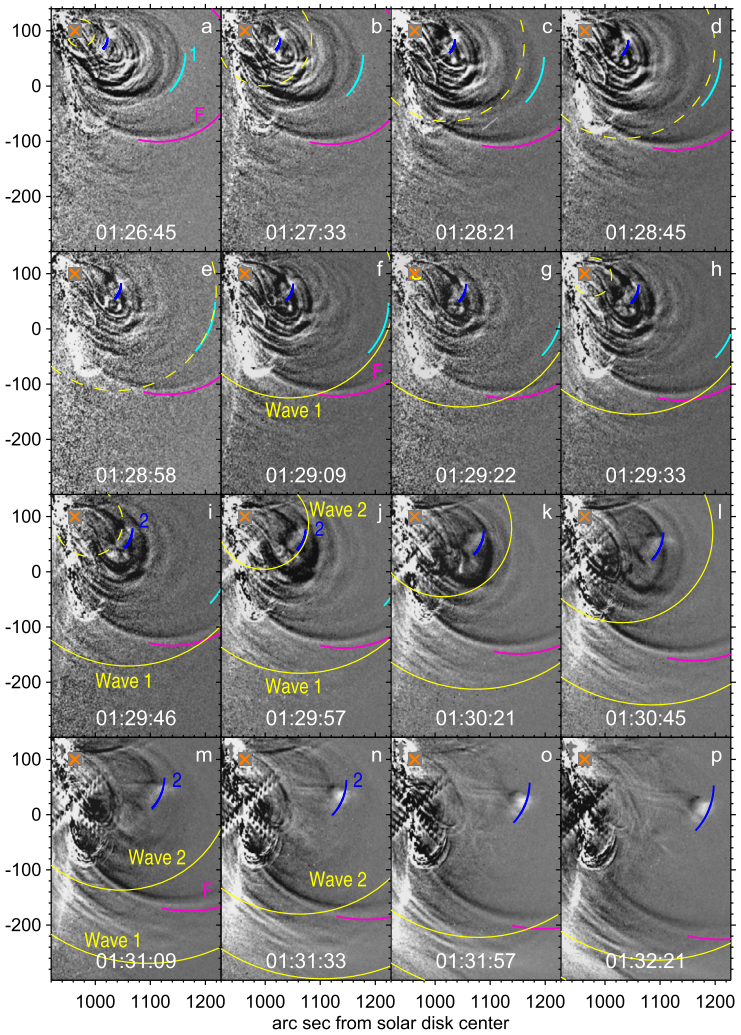

Figure 10 Erupting features 1 and 2 and the CME-bubble front along with the *yellow arcs* of the two presumable wavelike disturbances in SDO/AIA 193 Å running-difference images. The *cyan* and *blue arcs* outline their leading edges and the *magenta arc* outlines the CME-bubble front according to the kinematic plots in Figure 7. The *orange slanted cross* corresponds to origin O_1 denoted in Figure 3.

the characteristic fronts of the two wavelike disturbances denoted Wave 1 and Wave 2. The yellow-dashed arcs represent the imaginary propagation of their virtual, back-extrapolated predecessors from the point source denoted with the orange slanted cross. The initial speed of wave 1 at its detachment from the top of feature 1 (between Figures 10e and 10f) is 1140 km s^{-1}. The initial speed of wave 2 at its detachment from the top of feature 2 (just before Figure 10j) is 1950 km s^{-1}. These speeds correspond to normal fast-mode speeds over active regions and the higher initial speed of wave 2 relative to that of wave 1 is consistent with its appearance at a lower altitude, where the fast-mode speed is expected to be

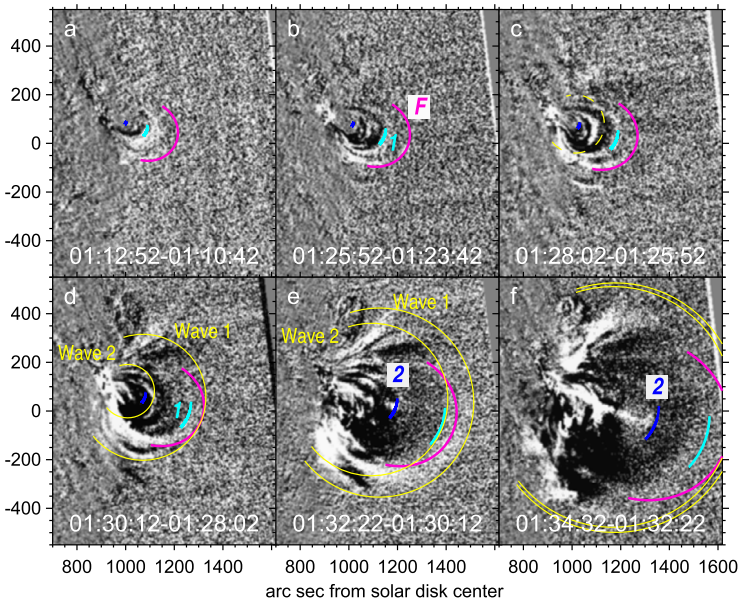

Figure 11 Eruptions *1* and *2* and the CME-bubble front *F* in PROBA2/SWAP 174 Å running-difference images. The *short-colored arcs* of the corresponding colors outline their leading edges according to the measurements. The *long yellow arcs* represent the derived positions of the two characteristic wavefronts.

higher. Note that the appearance and development of the near-surface EUV wave south of the eruption site in Figures 10k – 10p apparently corresponds to the propagation of wave 1.

Figure 11 follows these manifestations in PROBA2/SWAP 174 Å images that provide lower spatial and temporal resolution and sensitivity than AIA, but a wider field of view. These observations confirm that the CME-bubble front outlined with the magenta arc was the outermost structure of the future CME. The measurements taken of its flank from AIA images correspond to the expansion of its top where it can be detected. Erupting feature 1 is detectable in Figures 11b and 11c and possibly also in Figure 11d. Erupting feature 2 is visible in Figure 11e and even in Figure 11f at 01:34:32 that confirms its kinematic plots measured from AIA images only up to 01:33:00. Furthermore, Figures 11d – 11f confirm the correspondence between the development of the EUV-wave-like disturbances and the propagation of wave 1. The yellow ellipses of the characteristic wavefronts in these figures indicate that wave 2 is approaching wave 1 and will catch up with it shortly afterwards. Note that the centers of propagation of the two waves, as well as the eruption sites of features 1 and 2, appear to coincide in the plane of the sky, but could be separated at a considerable distance from each other along the line of sight.

Regarding the second acceleration pulse of erupting feature 1, it seems to be consistent with Figures 9 and 11. The total area of the acceleration profile is equal to the known speed of CME component 1. We estimate the uncertainty of the peak time of the second acceleration pulse to be within one minute. The duration and peak value are more uncertain, but unlikely to differ much from those of other acceleration pulses in Figures 7b and 9c. With all of these uncertainties, the acceleration–time plot of erupting feature 1 does not contradict the assumption made at the beginning of this section that the disturbance excited by each eruption propagated outward and accelerated all overlying coronal structures.

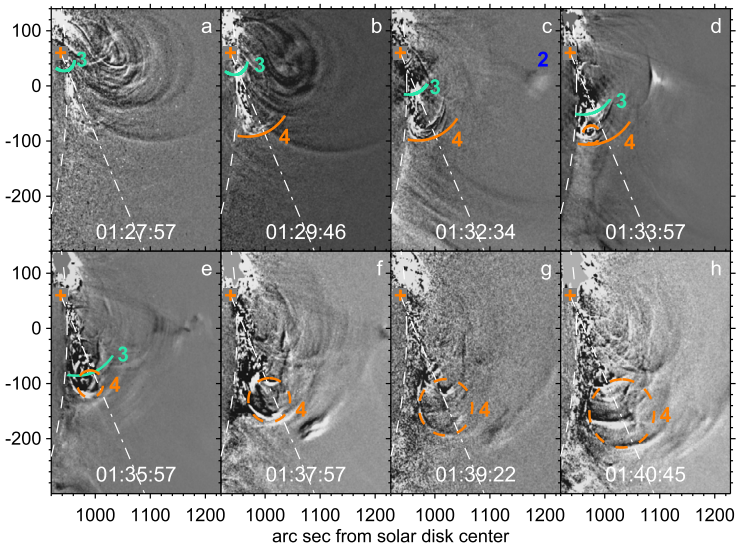

Figure 12 Motions near the limb observed in running-difference AIA 193 Å images. The *green arc* outlines the moving blob-like feature 3. The *orange arc* outlines the large loop-like structure 4 and the *orange-dashed circle* outlines its expanding outer boundary. The *dash-dotted line* (same as in Figure 3) corresponds to the direction of motion of feature 3 from origin O_2 denoted with the *orange cross*. The *white-dashed arc* denotes solar limb.

3.4. Motions Nearly Along the Limb

The characteristics and role of movements nearly along the limb, outlined in Figures 3b and 3c, remain unclear. Here we aim primarily to verify the suggestion of Shen et al. (2013) that these movements led to another fast CME.

Figure 12 shows the near-the-limb movements in more detail (see also the AIA94_eruptions.mpg movie in the Electronic Supplementary Material). While erupting feature 2 visible in Figure 12c rapidly moved away, a blob-like feature 3 appeared, outlined with the green arc. It moved at a small angle to the limb in the direction indicated by the dash-dotted line, towards a long loop-like structure 4 (possibly, a prominence; see Figure 1d). The southern edge of structure 4 is outlined with the orange arc. Having reached structure 4, feature 3 suddenly slowed down, while structure 4 began to expand. Its expanding outer boundary is outlined with the orange-dashed circle. Other complex movements were also observed that were not fast and were probably caused by the movement of feature 3, and some were its remnants. We focus on the movements of features 3 and 4 that appear to be the most significant.

These complexities make it difficult to use a one-dimensional temporal profile for measurements and interpretation, so we do not show it. Figure 13 shows the kinematic plots that we measured for the southern edges of these features with lower accuracy than previously. These movements give the impression that the motion of feature 3 was limited from the south and at the end of its movement it pushed structure 4, causing it to expand. The radial expansion speed of its outer boundary was about 100 km s^{-1} as long as it was detectable (until 01:45), and its center initially accelerated and decelerated soon afterwards. According to the online CDAW CME catalog (Yashiro et al. 2004: cdaw.gsfc.nasa.gov/CME_list/), the leading edge of the corresponding CME appeared at 3.6 $R_\odot$ three minutes later, at 01:48.

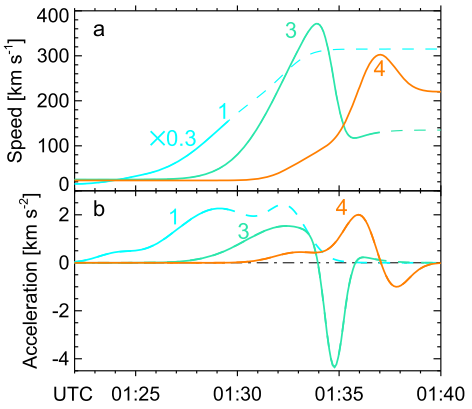

Figure 13 Speed–time (**a**) and acceleration–time (**b**) plots measured for near-the-limb moving features *3* and *4*. The measurements were made along the dash-dotted line in Figure 12. For comparison, kinematic plots for erupting feature *1* are shown with its speed–time plot reduced by a factor of 0.3. The *solid* parts of the curves correspond to the intervals in which the measured features were observed, and the *dashed* parts represent their presumable continuations.

Thus, features 3 and 4 were unlikely to become components of this fast CME, since their movements were too slow and too late.

The movement of the blob-like feature 3 is reminiscent of the rapid development of the flaring region in the SOL2001-08-25 event (Grechnev, Kochanov, and Uralov 2023). As in that event, the movement of feature 3 could be associated with the progressive detachment from the solar surface of the southwestern leg of the erupting magnetic-flux rope, whose top was feature 1. As Figure 13a indicates, the movement of feature 3 before its sharp deceleration was roughly synchronous with the movement of feature 1. The abrupt stop of feature 3 could correspond to the arrival of the detachment region at the unipolar base of the flux rope. This assumption is consistent with the limited extent of the flare arcade to the southwest (its boundary is indicated by the yellow-dotted arc in Figure 1d). The rising leg of the expanding flux rope likely pushed the loop-like prominence (feature 4), destabilizing it and causing it to erupt (Figures 1d – 1h). Its subsequent expansion was probably not fast and is not of interest to us.

To summarize, features 3 and 4 themselves are unlikely to have been involved in the fast CME, and their movements were likely driven by the main eruptions. Thus, the assumption that the movements nearly along the limb led to the second fast CME is not confirmed.

4. Waves and Type-II Burst

CME-associated shock waves are manifested in deflections of coronal streamers, which are detectable in difference coronagraph images, and their kinks (e.g. Uralova and Uralov 1994; Sheeley, Hakala, and Wang 2000) and/or in faint halos surrounding fast CME bodies as "second fronts" detectable in contrasted images (e.g., Vourlidas et al. 2003, 2013). Case studies confirmed the correspondence between both of these signatures and the same shock wave, and between its propagation and the trajectory of a Type-II burst (e.g., Grechnev et al. 2011, 2014b).

Here we use the same approach as in Section 3 and start in Section 4.1 with coronagraph observations. We then coordinate the measurements from LASCO images with the disturbances discussed in Section 3.3 to elucidate the history of the waves. In Section 4.2 we consider observations of wave signatures from different vantage points. Finally, in Section 4.3 we compare the results with observations of the Type-II radio emission.

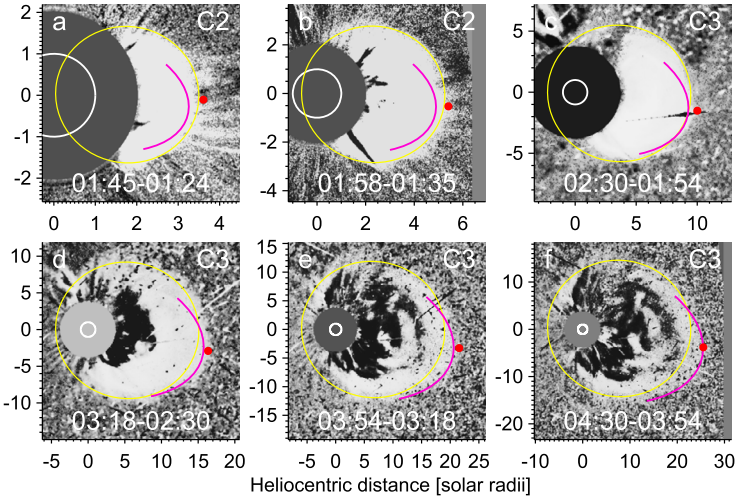

Figure 14 Wave halo, outlined with *yellow ellipses*, in enhanced-contrast running-difference LASCO-C2 and -C3 images. The *magenta arcs* outline the CME-body front (similar to Figure 4). The *red dots* represent measurements from the CDAW CME catalog. The fields of view of the images were progressively scaled to keep the visible size of the wave halo constant.

4.1. Manifestations of a Shock Wave in CME Images and Its History

To detect faint wave signatures in coronagraph observations, we use highly contrasted running-difference LASCO images. Figure 14 presents such images produced by LASCO-C2 and -C3. The wave trace appears here in the extensive elliptic halo surrounding the CME body. We fitted the wave expansion using the power-law pattern described in Section 3.3 with $t_{0\,\mathrm{Halo}} = 01{:}31{:}32$ and $\delta_{\mathrm{Halo}} = 2.65$. The yellow ellipses calculated using this fit acceptably match the wave halo, except for the CME nose and its near flanks in later images. To keep the apparent size of the halo in the figure constant, we progressively increased the field of view in the panels, also using this fit.

The magenta arcs in Figure 14 outline the front of the CME body, as done in Figure 4. These arcs approach the yellow ellipses outlining the halo in Figures 14a – 14c and are increasingly ahead of them in Figures 14d – 14f. This circumstance is consistent with the measurements in the CDAW CME catalog, represented by red dots (we fixed incorrect C2 timestamps in the data file provided in the CME catalog by replacing them with the final-correction times contained in the LASCO FITS files).

The kinematic plots of the wave signatures are presented in Figure 15 in comparison with those of the CME-body front shown in magenta (its expanded speed–time plot is shown in Figure 7a). We also applied our fit to the measurements from the CDAW CME catalog (symbols in Figure 15a). By setting the wave source at point O_1 at a distance of 1.01 $R_\odot$ from solar-disk center (Figure 3) and minimizing the nonlinearity of the distance–time plot in the log–log space, we found the onset time at 01:29:58, which differs from our estimate $t_{0\,\mathrm{Halo}} = 01{:}31{:}32$ by only 1.6 minutes. Then, applying a linear fit to this plot with the found onset time, we obtained $\delta = 2.84 \pm 0.01$ and the scaling factor with an accuracy of $\pm 4.6\%$ for the fastest feature ahead of the CME nose (red dots in Figure 14). Its speed–time plot is shown with the dotted curve in Figure 15b.

It is clear that the accuracy of all measurements is limited, that the CME-body front could begin to slow down a little towards the end of the measurements (see Gopalswamy

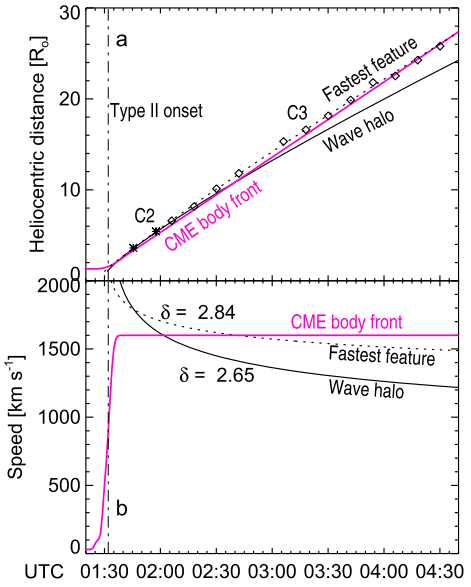

Figure 15 **a**) Distance–time plots of the wave halo (*black-solid*) and the CME-body front (*magenta*) in LASCO images in comparison with the refined measurements from the CDAW CME catalog (*symbols*). The dotted line represents the power-law fit of these measurements. **b**) Speed–time plots of the wave halo (*solid*), the fit of the measurements from the CME catalog (*dotted*), and the CME-body front (*magenta*). The *vertical dash-dotted line* marks the onset of the Type-II burst.

et al. 2013b), and so on. Despite all the uncertainties and simplifications and without yet considering the onset of the wave, the following conclusions can be drawn:

i) Judging by the propagation speed of the wave manifestations, this was a shock wave over almost the entire considered interval. This conclusion is confirmed by the fact that starting at 01:32 a Type-II burst was observed.
ii) Soon after the appearance and up to about 10 $R_\odot$, the kinematic characteristics of all wave manifestations corresponded to a freely propagating blast wave. For the wave halo this is also true later on.
iii) The leading part of the wave front ahead of the CME nose and its near flanks decelerated not as much as the wave halo, and its speed later approached the speed of the CME-body front. These signs indicate a transition of the shock wave to the bow-shock regime around the CME nose (see Grechnev et al. 2017 for more detail). The bow-shock regime becomes possible when the regime of the supersonic plasma flow around the wave driver is established (e.g., Bain et al. 2012; Grechnev, Kiselev, and Uralov 2022).

Even after a bow shock has formed, the wave front away from its driver resembles a blast wave. Here it is observed as the persisting wave halo.

Now there is enough information to reconstruct the entire history of the shock wave, starting from its origin. We found that two eruptions excited two wavelike disturbances with an actual interval of about one minute after each other. The second wave appeared below the first, followed it, approaching it, and had to catch up with it (see Figure 11). Each wave propagated from a region of high fast-mode speed to regions where it was lower. This should cause the disturbance profiles to steepen into shocks within a few minutes, depending on the accelerations of their drivers (Afanasyev, Uralov, and Grechnev 2013). A similar situation with two shock waves following each other was studied by Grechnev et al. (2011) when analyzing their Event 3. Figure 16 applies their considerations to our event, assuming that when the second wave caught up with the first, both shock discontinuities were already formed.

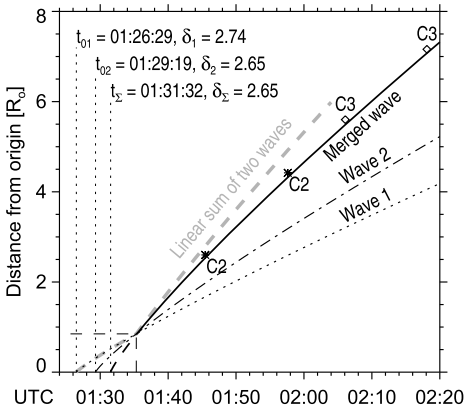

Figure 16 Merging of two nonlinear waves to form one, stronger wave. The *dotted* and *dash-dotted* curves represent the distance–time plots of the two initial waves, wave 1 and wave 2. The *gray-dashed* curve represents a plot of the resulting wave, calculated by linearly summing their speeds. The *black-solid* curve is the fit of the wave halo observed in LASCO images (Figures 14 and 15), and the *thick-dashed* portion represents the continuation to its virtual onset time t_Σ. The *thin-dashed* straight segments point to the intersection point at 01:35:19 at a distance of 0.85 $R_\odot$ from the origin. The *symbols* represent the refined measurements from the CDAW CME catalog.

A shock wave (here Wave 2) trailing a preceding one (here wave 1) must reach the leading front, so that the two shock waves merge and form a single shock front. Its speed is less than the sum of the speeds of the initial fronts (gray-dashed curve), but the resulting shock is stronger and faster than either of the original ones. The slope of its black-solid distance–time plot is steeper than those of the initial waves, and its apparent onset time [t_Σ] is later than of any of the initial waves. The parameters of the merged wave t_Σ and δ_Σ agree with LASCO observations. Hence, the wave halo observed in LASCO images was caused by a shock wave generated by the merger of the two preceding wavelike disturbances.

4.2. Observations of Wave Signatures from Different Vantage Points

The details of the shock-wave development have been revealed in Section 3.3 mainly from SDO/AIA observations with an imaging interval of 12 seconds. The eruption and accompanying phenomena occurred on the Sun's far side for STEREO-B, but were observed from STEREO-A on and above the solar disk. CME-associated wave-like disturbances appear in images as EUV waves (previously called "EIT waves"; see, e.g., Warmuth et al. 2001) that are detected mainly in the 195 Å EUVI channel. Figure 17 shows the EUV wave observed with STEREO-A/EUVI in 195 Å. EUV-wave analysis from these images is limited by its poor visibility and the long five-minute imaging interval, so we only consider the most obvious circumstances.

Judging by Figures 17a and 17b, the EUV wave appeared between 01:25:58 and 01:30:58. This is consistent with its actual appearance around 01:29:06, corresponding to the first acceleration peak of erupting feature 1 (without the correction for the propagation from the virtual point source). The onset time of the Type-II burst at 01:32 falls between Figures 17b and 17c, in which the wave reached the streamer at the western limb, where a Type-II source could be located. This disturbed streamer is also visible in the two subsequent images in Figures 17d and 17e.

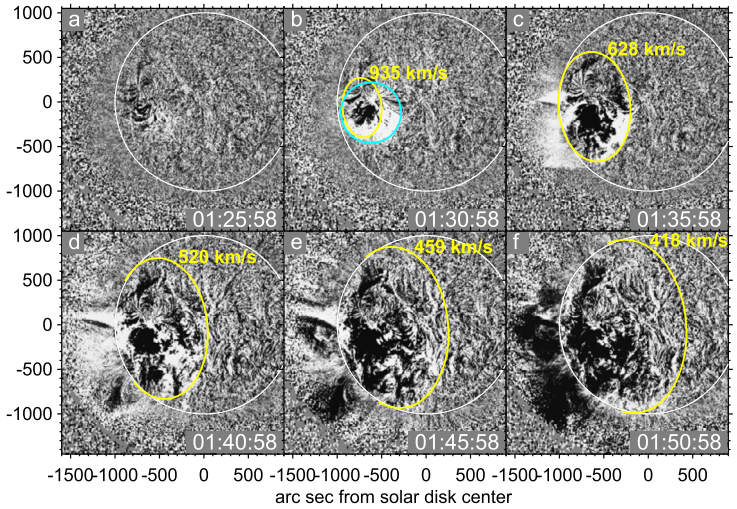

Figure 17 EUV wave visible in STEREO-A/EUVI 195 Å images. *Cyan circle* with a radius of 0.34 $R_\odot$ in panel **b** outlines the outer boundary of the first EUV-wave disturbance. *Yellow ellipses* correspond to the shock-wave propagation in an isotropic medium with $t_0 = 01{:}28{:}00$ and $\delta = 1.8$. *Yellow legends* indicate the EUV-wave speeds calculated from this fit. *White circles* denote solar limb. The times of the images were corrected to account for the light travel time from the Sun to Earth and STEREO-A.

The outermost boundary of the EUV wave in Figure 17b is circular, as Gopalswamy et al. (2013b) showed in their Figure 2a. However, the lower skirt of the EUV wave in subsequent images has a clearly elliptical shape. The initial circular EUV-wave front that appeared considerably to the east of the solar-disk center could not then transform into the elliptical fronts outlined by the yellow arcs in Figures 17c – 17f. Instead, it appears that two different waves were involved. Indeed, the second wave was excited by erupting feature 2 around 01:30:25 and most likely caused the inner part of the disturbance visible in Figure 17b, as well as the subsequent elliptical wavefronts.

The mentioned limitations of the EUVI observations make it difficult to accurately determine the fitting parameters to describe the EUV-wave propagation. Here we used $t_0 =$ 01:28:00 that is close to the earliest probable onset time of Wave 2 in Figure 9b (near the left edge of the yellow shading) and $\delta = 1.8$. The value of δ determines the wave deceleration and is more or less certain, as shown by the correspondence of the calculated yellow ellipses to the actual EUV-wave traces in Figures 17c – 17f. With a later wave onset time, the size of the yellow ellipse in Figure 17b decreases and the speeds of the elliptical fronts increase, but their deceleration remains. With $\delta = 1.8$, the exponent in the kinematic equation $x(t) \propto (t - t_0)^{2/(5-\delta)}$ is equal to 0.625 that is typical of EUV-wave propagation along the solar surface (e.g., Warmuth et al. 2001, 2004; Grechnev et al. 2011).

The consideration of the merging of two waves in the preceding section related to the plane of the sky, as viewed from the Earth's direction. In a real three-dimensional situation, the positions of the wave origins could be considerably spaced relative to each other. This possibility appears consistent with the displacement of the centers of the cyan circle and yellow ellipse relative to each other in Figure 17b. Therefore, the shape of the resulting wavefront could be complex, consisting of parts of three different ellipsoids, each of which expanded in its own way. Observations with the COR1 coronagraphs (Howard et al. 2008) on STEREO-B (located 117.6° behind the Earth) and STEREO-A (114.8° ahead of the

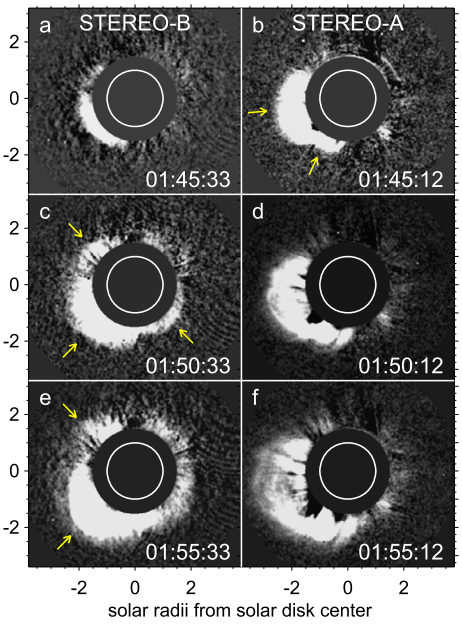

Figure 18 Wavefronts observed in STEREO-B/COR1 (*left*) and STEREO-A/COR1 (*right*) images. The *yellow arrows* in panels **b**, **c**, and **e** indicate parts of the wavefront that clearly do not conform to the shape of a simple ellipsoid. The *circles* outline solar limb. The nominal times of the images were not corrected.

Earth) in Figure 18 confirm this idea. This is particularly related to the parts of the wavefront indicated by the yellow arrows in Figures 18b, 18c, and 18e. Different wavefronts coexisting simultaneously are visible in the figure at least until 01:55.

Another conceivable option would be a single distorted wavefront. However, the intensity, extent, and shape of the shock front near the Sun are largely determined by the expanding CME's magnetic bubble. Therefore, sharp distortions of the shock front, such as those in Figure 18, should quickly disappear due to the effects of diffraction and nonlinearity. In any case, the shape of the wavefront in these images is much more complex than a single ellipsoid.

4.3. Type-II Emissions

A clear manifestation of a shock wave propagating in the corona is Type-II radio emission. It can be seen in dynamic spectra composed from the data from the Culgoora spectrograph (Prestage et al. 1994) and the *WAVES* spectrograph on STEREO-A (Bougeret et al. 2008). Figure 19a presents the initial part of the dynamic spectrum. A Type-II burst started at 01:32. This means that at least one shock discontinuity has already formed and reached a streamer at this time. Figure 19b presents the spectrum over a longer temporal interval and a wider frequency range.

In general, dynamic spectra represent a superposition of emissions coming from sources located in different places. The Type-II features appear to reflect a multi-ray coronal structure being traversed by a shock front. Here the Type-II structure is complex, suggesting the passage of a few shock waves. This especially applies to the metric Type-II burst. Knowing the t_0 and δ parameters of the possible shock waves involved, we aim to trace their frequency–time trajectories in the dynamic spectrum without trying to identify specific Type-II structures with a particular shock wave.

Three different pairs of curves (except for the thin-black-dotted curves in Figure 19b) denoted $[1_F, 1_H]$, $[2_F, 2_H]$, and $[3_F, 3_H]$ represent the Type-II trajectories for the fundamental

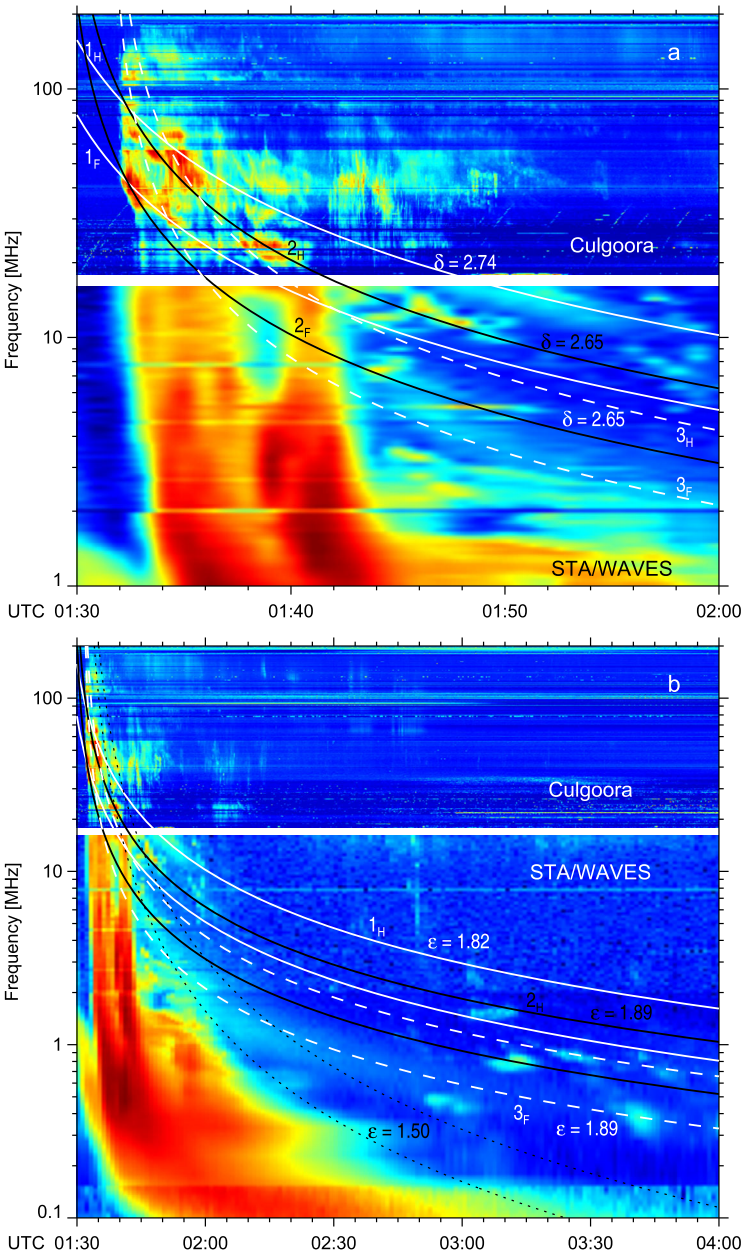

Figure 19 Type-II radio emission in the dynamic spectrum composed from the Culgoora and STEREO-A/*WAVES* data. The pairs of *curves* of different colors and line styles represent the Type-II trajectories for the fundamental and harmonic emissions calculated for three different shock waves. **a**) Initial interval. The density-falloff exponents δ corresponding to different trajectories are specified. **b**) Longer temporal interval and wider frequency range. The frequency-drift-rate exponents $\varepsilon = 5/\delta$ are specified. The *black-dotted curves* represent hypothetical Type-II trajectories for the frequency-drift-rate exponent $\varepsilon = 1.50$.

and harmonic emissions. They were calculated for the propagation of three different shock waves using the power-law pattern described in Section 3.3 (for more details see Grechnev, Kochanov, and Uralov 2023). The corresponding values of δ are indicated for each pair in Figure 19a. The trajectories match the frequency-drift rates of the Type-II bands in the decametric-hectometric (DH) range, without contradicting the slopes of metric Type-II structures. Besides continuous bands, the trajectories also correspond to some blob-like features (cf. Cane and Erickson 2005).

The STEREO-A/*WAVES* spectrum in Figure 19a shows two decametric Type-III bursts, one at 01:33 – 01:37 and the other at 01:40 – 01:42. The first one started in the metric range as a group of Type-III bursts, temporally corresponded to the second acceleration of the CME-bubble front F (Figure 7) and the sharp movements of near-the-limb erupting features 3 and 4 (Figure 13), and thus could have been associated with the eruption process. The second Type-III burst starting at about 01:40 without conspicuous continuation into the metric range, occurred after the revealed acceleration episodes and appears to indicate the release of accelerated electrons that had previously been trapped in the expanding flux rope. The Type-III-emitting electrons are likely to be proton tracers, so the release of protons trapped in the flux rope could have begun at the same time. The onset time of this Type-III burst is indeed close to the particle release time estimated from the velocity-dispersion analysis by Gopalswamy et al. (2013b) at 01:40 and by Rouillard et al. (2016) at 01:37:20. Note that the bow-shock regime ahead of the CME nose was not yet established at that time (see Section 4.1 and Figure 15b). The top of the first erupting structure reached at that time a distance of about 1 $R_\odot$ from the eruption site (Figure 9a). These circumstances are discussed in Section 6.

The STEREO-A/WAVES spectrum in Figure 19b does not show any Type-III bursts in the interval 02:00 – 02:10 at frequencies between 1 and 14 MHz that Shen et al. (2013) revealed in the *Wind*/WAVES spectrum and considered as a possible indication of the interaction between two shocks driven by two presumable CMEs. We note that these Type IIIs were only observed by *Wind*/WAVES, but not by any of the WAVES spectrographs on STEREO-A or STEREO-B. This is possible if the source of these Type IIIs was located not far from the Sun–Earth line and was visible only to *Wind*/WAVES located at Lagrangian point L1. On the other hand, the development of the CME was entirely in the field of view of STEREO-A and from its vantage point nothing could be missed. These circumstances contradict the idea of Shen et al. (2013).

In fact, these authors based their considerations on the assumption that a bow shock was excited by a fast CME. However, the shock-wave development turns out to be more complex, from a piston shock to a blast wave and then to a bow shock. This scenario is further complicated by the merging of two shock waves into a single, stronger one, occurring differently in different directions. The Type-II emissions presented in Figure 19 confirm these circumstances. We have not found in the dynamic spectra any drifting features with $\delta \approx 2.84$ corresponding to the bow-shock propagation (see Figure 15). This may indicate that the sources of the observed Type-II emissions in this event were located on the shock flanks rather than ahead of the CME nose.

There is another issue related to wide-range dynamic spectra. It is known that the dependence of the Type II's drift rate $[\mathrm{d}f/\mathrm{d}t]$ on frequency $[f]$ is proportional to the power of frequency $\mathrm{d}f/\mathrm{d}t \propto -f^{\epsilon}$, where ϵ is a characteristic exponent. The question is the value of this exponent. Grechnev, Kochanov, and Uralov (2023) have shown that ϵ is related to the density-falloff exponent δ as $\epsilon = 5/\delta$ and that ϵ is typically between 5/3 and 2. The value of ϵ less than 5/3 is doubtful, since with $\delta > 3$ the shock wave is expected to accelerate, which is especially unlikely at large distances from the Sun.

Several studies examined the relationship between the frequency-drift rate of Type-II bursts and their starting frequencies. The estimate of ϵ in this approach is biased towards smaller values. For example, Shanmugaraju, Moon, and Vrsnak (2009) found for the relationship between the mean frequency and the drift rate of metric Type IIs the exponent of 1.88 – 1.89 and for the relationship between their starting frequency and the drift rate the exponent of 1.37. For a representative set of 128 events with starting frequencies from 420 MHz to 30 MHz Umuhire et al. (2021) found $\epsilon = 1.33$. The starting frequency of a Type-II burst would be a significant parameter if the shock was initially excited as a bow shock ahead of a fast CME (Lin, Mancuso, and Vourlidas 2006; Gopalswamy et al. 2013a). However, in the case of impulsive piston-shock excitation, the starting frequency is determined by the distance between the wave origin and the Type-II source (see, e.g., Figure 10 in Grechnev et al. 2014b) and does not seem to be an important quantity.

Leaving aside the question of the starting frequency, we consider frequency-drift rates in the spectrum shown in Figure 19b. Here, actual values of ϵ of 1.82 and 1.89 are specified for Type-II bands. In addition, the black-dotted pair of curves represents a hypothetical situation with $\epsilon = 1.50 < 5/3$. These trajectories are considerably steeper than actual Type-II drift rates that is especially noticeable at frequencies below 1 MHz.

To summarize, Type-II manifestations in dynamic spectra are consistent with the measurements, considerations, and conclusions in the preceding sections, both qualitatively and quantitatively. All this confirms the complex history of the shock wave, reconstructed from observations.

5. Relationship Between Observed Phenomena and Magnetic Reconnection

We have not yet considered the relationship between identified eruptions and flare emissions. According to widely accepted solar-flare models, this relationship is generally determined by magnetic reconnection. In the classical two-dimensional CSHKP model (Carmichael 1964; Sturrock 1966; Hirayama 1974; Kopp and Pneuman 1976), reconnection leads to the formation of flare loops and the acceleration of particles that produce intense flare emissions. According to three-dimensional considerations and observational studies, reconnection supplies poloidal magnetic flux into the forming flux rope, causing its accelerated expansion (e.g., Inhester, Birn, and Hesse 1992; Fletcher and Hudson 2001; Longcope and Beveridge 2007; Qiu et al. 2007; Miklenic, Veronig, and Vršnak 2009; Tschernitz et al. 2018). Specifically, the relation between X-ray emission and CME acceleration was demonstrated by Zhang et al. (2001) and by Temmer et al. (2008, 2010). The relation between reconnection rate and CME acceleration was demonstrated by Qiu et al. (2004). The relation between reconnection and X-ray emission was demonstrated by Grechnev, Kochanov, and Uralov (2023) and by Corchado Albelo, Kazachenko, and Lynch (2024). And in our event, a correspondence is also expected between the accelerations of the erupting structures, the magnetic-flux change rate, and the intensity of hard X-ray (HXR) emission. However, there are some difficulties in establishing such a correspondence in this event.

The reconnected magnetic flux is usually measured from magnetograms by referring to the flare ribbons that are identified from Hα or ultraviolet images (e.g., Miklenic, Veronig, and Vršnak 2009; Tschernitz et al. 2018) or by calculating the total magnetic flux covered by the post-eruption arcade observed in EUV (Chertok et al. 2013; Gopalswamy et al. 2017). Using the SDO/AIA observations in the 1600 Å channel, which is best suited for identifying

flare ribbons, Kazachenko et al. (2017) assembled a flare-ribbon database for events that occurred within 45° from solar-disk center. However, this extensive database does not contain our near-the-limb event, nor does it contain data on the magnetic-flux change rate.

The AIA images in the 1600 Å channel produced on 17 May 2012 suffer greatly from severe blooming because of high brightness of the ribbons. This distortion occurs when the charge in a pixel of the photodetector exceeds the saturation level and fills adjacent pixels, resulting in false brightenings near bright areas in the image. We used instead images in the 1700 Å channel, where the brightness of the ribbons is lower and blooming is less pronounced. Areas of obvious blooming were marked manually and then not included in the calculations.

Another difficulty is caused by the location of the flare site in this event near the limb, where line-of-sight (LOS) magnetograms are highly distorted, because the radial magnetic component [B_r] is equal to the LOS component [$B_{\rm LOS}$] only along the Sun–Earth line with the observing angle $\theta = 0$. Therefore, we calculated B_r from a vector magnetogram (although it is also imperfect near the limb). Full-disk vector magnetic-field data are routinely provided by the *Helioseismic and Magnetic Imager* (HMI: Scherrer et al. 2012) on board SDO and information about the full magnetic vector [$\boldsymbol{B}$] is contained in the hmi.B_720s series data accessible at the *Joint Science Operations Center* (JSOC).

The components of the $\boldsymbol{B}$ vector were calculated as $B_x = |B| \cos\theta$, $B_y = |B| \sin\theta \sin\phi$, and $B_z = -|B| \sin\theta \cos\phi$, where $|B|$ is the magnetic-field magnitude, θ is inclination, and ϕ is azimuth. The azimuth determines the direction of the transverse magnetic-field component (Sun 2013). The disambig file contains information about the resolved 180°-ambiguity of the magnetic-field component transverse to the LOS (Harvey 1969). The radial magnetic-field component was calculated at each point as the scalar product $B_r = \boldsymbol{B} \cdot \boldsymbol{u}$, where $\boldsymbol{u}$ is the unit vector normal to the solar surface.

These measures have been taken to overcome the above problems, but the quality of the final result is difficult to guarantee. The reconnected magnetic flux was found in the usual way by calculating the total positive and total negative magnetic flux within the cumulative area covered by the flare ribbons at the current time. Then differentiation of the cumulative magnetic flux provided the magnetic-flux change rate shown in Figure 20b. For comparison, Figure 20a presents the measured accelerations of all identified moving features.

The maximum reconnection rate we measured with an imaging interval of 24 s is 8.7×10^{18} Mx s^{-1}. The statistical pattern established for eruptive flares by Tschernitz et al. (2018) in their Table 4 and Figure 7 based on one-minute observations predicts for the M5.1 GOES importance of our event a peak reconnection rate of 5.3×10^{18} Mx s^{-1}. Approaching our measurements in steps of 24 s to those of Tschernitz et al. (2018), the maximum reconnection rate, smoothed by width three, is 6.8×10^{18} Mx s^{-1}, which is close to their statistical result.

The *Konus Gamma-Ray Burst Experiment* (*Konus* or *Konus–Wind*: Aptekar et al. 1995) on board the *Wind* mission observed the HXR burst in the waiting mode from 01:24 till 01:44 at a temporal sampling of 2.944 s with a gap between 01:32:30 and 01:34:00. Figure 20c shows the temporal profiles recorded with *Wind/Konus* in two of its three energy bands. The impulsive phase of the flare started at 01:27, in agreement with the impulsive-acceleration stage of the eruptive event (see Section 3.2). The increases in HXR emission are qualitatively consistent with increases in the reconnection rate during the impulsive phase, whose completion was not observed by *Konus*. The discrepancy in the relationship between the magnitudes of some HXR peaks and the reconnection-rate peaks is probably caused by the discussed problems with our measurements.

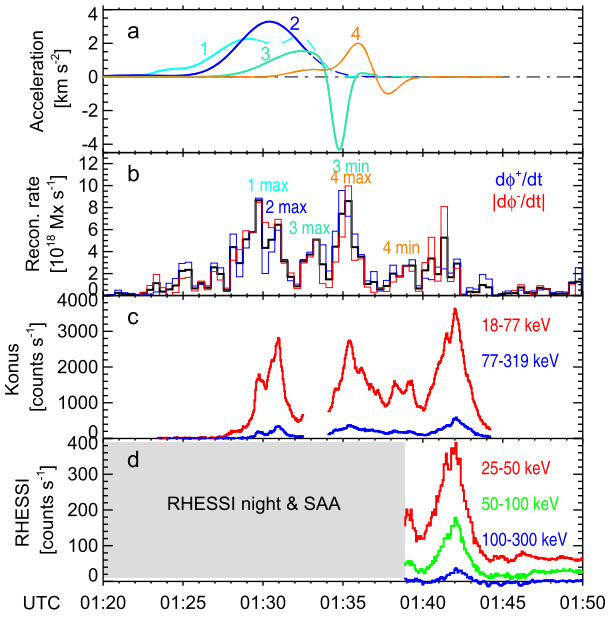

Figure 20 Comparison of temporal profiles of different characteristics of the event. **a**) Accelerations of erupting features 1, 2, 3, and 4. **b**) Temporal profiles of the magnetic-flux change rate. The *thin-blue line* presents the positive polarity, the *thin-red line* presents the negative polarity by the absolute value. The *thick-black line* presents the average of the two polarities. The *color labels* indicate maxima and minima of acceleration pulses corresponding to increases in the magnetic-flux change rate. **c**) HXR burst observed by *Wind*/*Konus*. **d**) RHESSI observations of the final part of the HXR burst. Its preceding part was missed (*gray shading*). RHESSI background levels are shifted up by 25 (50 – 100 keV) and 50 (25 – 50 keV) to show the burst better.

RHESSI missed most of the flare because of the night and the passage in the South-Atlantic Anomaly (SAA) and resumed observations shortly before 01:39. Background variations in several preceding and subsequent orbits were fitted for each energy band and subtracted from the actual count rates. The net temporal profiles recorded in three RHESSI bands in Figure 20d indicate the termination of the impulsive phase at about 01:45, when reconnection ceased. In the interval 01:39 – 01:44 observed by both *Wind*/*Konus* and RHESSI, the HXR intensity variations in their close energy bands are similar to each other.

The impulsive phase of the flare corresponded to the interval of considerable reconnection rate and strong accelerations of erupting structures. One can find an approximate correspondence between peaks of acceleration and deceleration in Figure 20a and increases in the reconnection rate in Figure 20b (colored labels). The reconnection-rate peaks “1 max” and “2 max”, temporally close to the maximum accelerations of erupting features 1 and 2, were probably associated with the formation of magnetic-flux ropes. This is unlikely for features 3 and 4; here, reconnection episodes could have been forced by abrupt changes in the movements of their near-surface parts. The second (dashed) acceleration of feature 1 was caused by the passage of a disturbance (Wave 2) through its upper part and is unlikely to be related to reconnection. We were unable to identify a counterpart to the last triple peak of the reconnection rate at 01:40 – 01:42 among the movements of erupting structures, while the corresponding HXR peak was strong. It was observed by RHESSI that made it possible to locate its source.

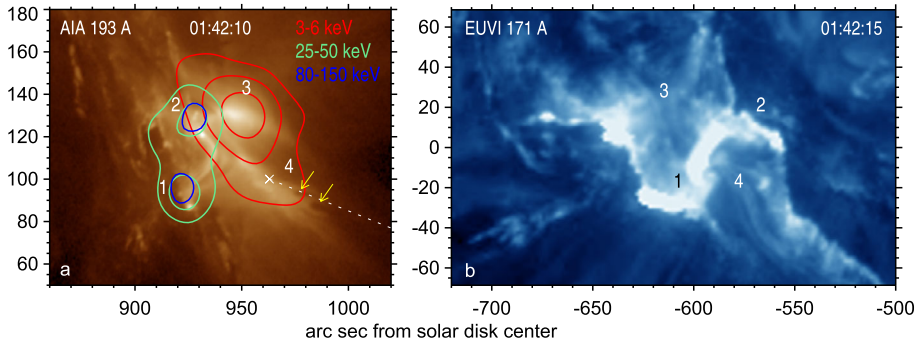

Figure 21 Flare region during the last HXR peak observed from the Earth's direction (**a**) and from the STEREO-A vantage point (**b**). The contours in panel **a** represent the images produced by RHESSI in three energy bands specified. Contour levels are [0.27, 0.5, 0.8] for 3 – 6 keV, [0.5, 0.8] for 25 – 50 keV, and 0.8 for 80 – 150 keV. The *dotted line* (same as in Figures 3 and 5) indicates the direction of motion of the main erupting structures, measured from origin O_1 (*slanted cross*), denoted in Figure 3. The *yellow arrows* indicate dark downflowing voids. *Labels 1 – 4* denote four specific regions in panel **a** and their possible counterparts in panel **b**.

Figure 21 shows the flare region visible from two vantage points during the HXR peak at 01:42. Figure 21a (similar to Figure 3 in Firoz et al. 2017) presents an SDO/AIA 193 Å image overlaid with contours of RHESSI images synthesized from data accumulated from 01:41:30 to 01:42:30. The basic set of contour levels is [0.27, 0.5, 0.8]; for higher energies, we use higher levels from this set according to the increasing background contribution. Figure 21b shows a simultaneous STEREO-A/EUVI 171 Å image (same as in Figure 1h). The four X-ray-emitting regions are labeled 1 – 4 in Figure 21a. Their probable counterparts in Figure 21b were determined from the analysis of the observed groups of flare loops and the corresponding flare ribbons.

Regions 1 and 2 at the bases of the low loops visible in 193 Å emitted strong hard X-rays up to 80 – 150 keV. Both high-temperature regions 3 (19 MK) and 4 (13 MK), emitting thermal X-rays, were located in the corona. These hot regions are bright in 193 Å due to the high-temperature FeXXIV window in the temperature response function of this channel (Lemen et al. 2012). When viewed from STEREO-A, regions 3 and 4 are projected between the flare ribbons. The location of the HXR sources and associated coronal loops during the peak at 01:42 indicates their connection with region 4. These loops and region 4 were arranged along the direction of motion of eruptions 1 and 2, indicated by the dotted line in Figure 21a. Therefore, this HXR peak was probably associated with an additional reconnection episode in the wake of the CME.

Region 3 was associated with another group of indistinct loops, whose western bases were on the northern ribbon in Figure 21b. These loops, clearly visible in the AIA 131 Å image presented by Firoz et al. (2017) in their Figure 3a, were probably formed in one of the previous episodes.

Both the hot regions and the arcade below them gradually rose, as expected during flare reconnection. Firoz et al. (2017) found from RHESSI data the rise of region 3 between 01:42 and 01:58 at a speed of 14 km s^{-1} for a source of 6 – 12 keV and 15 km s^{-1} for a higher source of 12 – 18 keV. For the top of the arcade below region 4, we estimated rise at a speed of 7.5 km s^{-1} during 01:48 – 02:28.

Starting at 01:40 and continuing until at least 02:00, AIA 193 Å images show downward flows of bright material and dark voids onto the developing post-eruption arcade, a phe-

nomenon discovered by McKenzie and Hudson (1999). These motions are demonstrated by the AIA193_downflows.mpg movie in the Electronic Supplementary Material. Note that the movie was composed from AIA 193 Å images with varying exposure times, so some visible local brightenings are due to saturation effects. Although the mechanism of void formation is still unclear, its direct connection with the plasma outflow from the reconnection site is undoubted (McKenzie 2000; Linton and Longcope 2006). The discrete nature of supra-arcade downflows in space and time indicates that coronal magnetic reconnection is highly localized, being patchy and bursty. As Khan, Bain, and Fletcher (2007) found, relative timing indicates their first appearance during HXR bursts in the vast majority of observations (90%), as in this event.

6. Discussion and Concluding Remarks

As often happens, despite the apparent abundance of observations of this event, their limitations made it difficult to identify and measure significant features and understand its development. The SDO/AIA field of view is insufficient. PROBA2/SWAP images lack sensitivity and imaging rate. The SDO/HMI magnetograms are of insufficient quality near the limb. Hard X-ray observations are limited. By combining observational data from different instruments and relying on the results of studies in recent years, it was possible to take the next step in understanding the course of this event.

A distinctive feature of our study is the measurement of the movements of structures involved in the eruption process. The results of these measurements made it possible to establish the sequence of phenomena and identify cause-and-effect relationships between them. Together with the obtained quantitative characteristics, they complement and clarify the picture of the event outlined by previous studies. Some of their results and conclusions are confirmed. Some others are refined. Some more measurement results reveal differences in the development of the event from the assumptions made in previous studies.

Indeed, as Shen et al. (2013) concluded, there were two eruptions in this event. The actual interval between them was as short as 1.3 minutes. Both erupting structures moved one after the other in the same direction in the plane of the sky, as viewed from the Earth's direction. Both of these structures then became components of a single CME, contrary to the idea of two CMEs proposed by Shen et al. (2013). The bump moving nearly along the limb that these authors considered to be associated with the second CME was in fact at the bottom of the leg of the first erupting structure and was moving towards its base. Since there was only one CME, the twin-CME scenario proposed by Li et al. (2012) is unlikely to be relevant to this event.

Our measurements also confirm the assumption of Shen et al. (2013) about the presence of two shock waves, but their excitation mechanism differed from what the authors assumed. The main cause of the expansion of coronal structures during the CME formation, as well as the excitation of wavelike disturbances, is the sharp impulsive expansion of erupting structures. The subsequent steepening of the wavelike disturbance due to the steep decline in the fast-mode speed leads to the rapid formation of a shock discontinuity. The components of this scenario have been identified in observations and verified in simulations and theoretically (e.g., Temmer et al. 2009; Afanasyev, Uralov, and Grechnev 2013; Vršnak et al. 2016; Uralov, Grechnev, and Ivanukin 2019).

In this event, each of the two eruptions caused a disturbance that, propagating outward, accelerated all the structures above it. The two disturbances steepened into piston shocks and then merged into one, stronger shock. The shock then propagated as a blast wave for

some time and at distances of about 10 $R_\odot$ began to transform into a bow shock ahead of the CME nose and its near flanks.

When the first erupting structure reached a distance of about 1 $R_\odot$, dynamic radio spectra show a Type-III burst that started at 01:40. Type-III bursts indicate the escape of accelerated electrons into the interplanetary space. The onset time of this late-phase Type-III burst is close to the proton release time obtained by Gopalswamy et al. (2013b) and Rouillard et al. (2016) from the velocity-dispersion analysis.

Cane, Richardson, and von Rosenvinge (2010) found that the Type IIIs in least-intense, electron-rich impulsive proton events occurred during the flare's impulsive phase, while in the largest gradual SEP events, the Type IIIs occurred after the impulsive phase. A model for the escape of flare-accelerated particles proposed by Masson, Antiochos, and DeVore (2013) apparently relates to this property of gradual SEP events. In this scenario, flare-accelerated protons do not escape the flare site directly, but after being injected into the erupting flux rope. The injected particles then remain trapped in the expanding flux rope until it reconnects with an open magnetic structure, when they gain access to the interplanetary space. This scenario was supported by Kocharov et al. (2017) and Grechnev et al. (2017). The last study found that the particle-release times estimated by Reames (2009) from the velocity-dispersion analysis, for most of the events he examined were close to the onset times of decametric Type IIIs. It was also noted that due to the difference in the lifetimes of 100 MeV protons and 0.5 MeV electrons in the same plasma by two orders of magnitude, the electron-to-proton ratio for the particles escaping from a flux rope with an initial density of $n > 10^{10}$ cm^{-3} may be much less than when they directly escape from the flare site in an impulsive event. This scenario also explains why confined flares are not proton-rich. Thus, the role of CMEs in the appearance of energetic solar protons may be twofold: i) acceleration of protons by the associated shock wave and ii) provision of release for flare-accelerated protons. Both aspects are important for SEPs and GLEs.

The ellipsoidal shape of the single-shock front considered by Rouillard et al. (2016) seems adequate. However, the initial presence of different wavefronts dramatically complicates 3D reconstructions for those times. Moreover, the different wavefronts in this event were not clearly visible. It seems promising to study similar phenomena in other events, perhaps using simpler methods.

The applicability of the authors' approach before establishing the bow-shock regime and the relevance of the corresponding conclusions to this event are not obvious. Shock waves are easily excited as piston shocks by an impulsive mechanism when the fast-mode speed in the environment is not crucial (Vršnak and Cliver 2008). Piston shocks appear both in weak events and in the absence of any CME (Nitta et al. 2013; Grechnev et al. 2022). The shock wave is then detached from the piston and propagates further as a blast wave. The relationship between the piston (CME) speed and the ambient fast-mode speed determines the subsequent history of the shock wave: If the CME is fast, then the shock wave transforms into the bow shock; if the CME is slow or absent, then it decays into a weak disturbance. These circumstances should not be overlooked in future studies.

Another point that is sometimes overlooked is about Type-II bursts. To generate narrow-band Type-II emission, its source must be compact in height, otherwise the emission from extended regions with different plasma densities will produce a continuum (Knock and Cairns 2005). A suitable source of Type-II emission is a streamer. When crossing a streamer, the shock causes a flare-like process in its current sheet that runs along the streamer and generates the Type-II emission. In this situation, a Type-II burst starts when an already existing shock wave reaches the streamer and not when the shock discontinuity starts to form. This option is confirmed by a number of features of Type-II bursts observed in individual cases,

such as Type-IIs with a C-like onset, Type-IIs with bidirectional frequency drift, and multi-band Type-IIs.

The flare in this event looks like an ordinary two-ribbon flare, complicated due to the two eruptions by the presence of additional ribbons parallel to the main ribbons. Besides, weak remote ribbon-like structures were also observed. The magnetic-flux change rate is roughly similar to the hard X-ray burst, as observed previously (e.g., Miklenic, Veronig, and Vršnak 2009). The ratio of the maximum magnetic-flux change rate and the M5.1 flare importance is close to the statistical pattern found by Tschernitz et al. (2018). There is also an approximate correspondence between the magnetic-flux change rate and the accelerations or decelerations of erupting structures, as expected (e.g., Vršnak 2016). However, some abrupt changes in their movements were unlikely to be associated with the formation of magnetic-flux ropes; it is possible that these changes were the cause of the reconnection episodes. This issue deserves further study. Some other aspects of this flare, such as the magnetic configuration, the atypical microwave burst, and its relation to magnetic reconnection, are discussed in Article II.

To summarize, the SOL2012-05-17 event was representative, as a number of its constituent phenomena were observed in other events. In this sense, this event can serve as a guide for studies of eruptive flares. However, some components of the picture of this event differ from what is often assumed, and some others have not previously been noted. While our analysis was based on simple considerations, mainly limited to two dimensions, we anticipate future in-depth studies of the issues raised.

Supplementary Information The online version contains supplementary material available at https://doi.org/10.1007/s11207-024-02373-0.

Acknowledgments We thank A.A. Kochanov, I.I. Myshyakov, and A. Warmuth for useful discussions and Y. Kubo and N.P. Prestage for the dynamic spectra used here. We appreciate all authors who have previously studied this event, thereby contributing to knowledge about it. We thank the anonymous reviewer for valuable remarks and suggestions that helped improve the original manuscript.

We are grateful to the NASA/SDO and the AIA and HMI science teams; the NASA's STEREO/SECCHI science and instrument teams; the teams operating SOHO/LASCO, S/WAVES, the *Wind*/*Konus* team at the Ioffe Institute, and the team that operated RHESSI for the data used here. We thank the team maintaining the CME Catalog at the CDAW Data Center by NASA and The Catholic University of America in cooperation with the Naval Research Laboratory. SOHO is a project of international cooperation between ESA and NASA.

Author contributions N.M. prepared images for the initial analysis, processed and analyzed RHESSI data. A.L. restored and analyzed Wind/Konus data. K.F. measured the movements of erupting features, contributed to their interpretation and to the analysis of RHESSI observations. V.K. measured the manifestations of waves and the reconnected magnetic flux and monitored hard X-ray data. A.U. interpreted the observations and measurement results. V.G. coordinated the study, performed other measurements, and drafted the manuscript. All authors reviewed the manuscript.

Funding This study was financially supported by the Ministry of Science and Higher Education of the Russian Federation. K.A. Firoz was supported by the National Natural Science Foundation of China (12233012, 12333010). A.L. Lysenko was supported by the basic funding program of the Ioffe Institute No. FFUG-2024-0002.

Data Availability The datasets analyzed during the current study were derived from the following public domain resources: Virtual Solar Observatory sdac.virtualsolar.org/ Joint Science Operations Center jsoc.stanford.edu/ The Proba2 Science Center proba2.sidc.be/swap/data/bsd/ NASA's Space Physics Data Facility (SPDF) spdf.gsfc.nasa.gov/pub/ SOHO LASCO CME CATALOG cdaw.gsfc.nasa.gov/CME_list/ The Wind/Konus waiting-mode data used in this study are available from A.L. Lysenko on reasonable request.

Declarations

Competing interests The authors declare no competing interests.

References

Afanasyev, A.N., Uralov, A.M., Grechnev, V.V.: 2013, Propagation of a fast magnetoacoustic shock wave in the magnetosphere of an active region. *Astron. Rep.* **57**, 594. DOI. ADS.

Anastasiadis, A., Lario, D., Papaioannou, A., Kouloumvakos, A., Vourlidas, A.: 2019, Solar energetic particles in the inner heliosphere: status and open questions. *Phil. Trans. Roy. Soc. London Ser. A* **377**, 20180100. DOI. ADS.

Aptekar, R.L., Frederiks, D.D., Golenetskii, S.V., Ilynskii, V.N., Mazets, E.P., Panov, V.N., Sokolova, Z.J., Terekhov, M.M., Sheshin, L.O., Cline, T.L., Stilwell, D.E.: 1995, Konus-W gamma-ray burst experiment for the GGS Wind spacecraft. *Space Sci. Rev.* **71**, 265. DOI. ADS.

Aschwanden, M.J.: 2012, GeV particle acceleration in solar flares and ground level enhancement (GLE) events. *Space Sci. Rev.* **171**, 3. DOI. ADS.

Bain, H.M., Krucker, S., Glesener, L., Lin, R.P.: 2012, Radio imaging of shock-accelerated electrons associated with an erupting plasmoid on 2010 November 3. *Astrophys. J.* **750**, 44. DOI. ADS.

Battarbee, M., Guo, J., Dalla, S., Wimmer-Schweingruber, R., Swalwell, B., Lawrence, D.J.: 2018, Multi-spacecraft observations and transport simulations of solar energetic particles for the May 17th 2012 event. *Astron. Astrophys.* **612**, A116. DOI. ADS.

Berghmans, D., Hochedez, J.F., Defise, J.M., Lecat, J.H., Nicula, B., Slemzin, V., Lawrence, G., Katsyiannis, A.C., van der Linden, R., Zhukov, A., et al.: 2006, SWAP onboard PROBA 2, a new EUV imager for solar monitoring. *Adv. Space Res.* **38**, 1807. DOI. ADS.

Bougeret, J.L., Goetz, K., Kaiser, M.L., Bale, S.D., Kellogg, P.J., Maksimovic, M., Monge, N., Monson, S.J., Astier, P.L., Davy, S., et al.: 2008, S/WAVES: The Radio and Plasma Wave Investigation on the STEREO mission. *Space Sci. Rev.* **136**, 487. DOI. ADS.

Brueckner, G.E., Howard, R.A., Koomen, M.J., Korendyke, C.M., Michels, D.J., Moses, J.D., Socker, D.G., Dere, K.P., Lamy, P.L., Llebaria, A., et al.: 1995, The Large Angle Spectroscopic Coronagraph (LASCO). *Solar Phys.* **162**, 357. DOI. ADS.

Bruno, A., Bazilevskaya, G.A., Boezio, M., Christian, E.R., de Nolfo, G.A., Martucci, M., Merge', M., Mikhailov, V.V., Munini, R., Richardson, I.G., et al.: 2018, Solar energetic particle events observed by the PAMELA mission. *Astrophys. J.* **862**, 97. DOI. ADS.

Cane, H.V., Erickson, W.C.: 2005, Solar type II radio bursts and IP type II events. *Astrophys. J.* **623**, 1180. DOI. ADS.

Cane, H.V., Richardson, I.G., von Rosenvinge, T.T.: 2010, A study of solar energetic particle events of 1997 – 2006: their composition and associations. *J. Geophys. Res. Space Phys.* **115**, A08101. DOI. ADS.

Carmichael, H.: 1964, A process for flares 50. NASA, Science and Technical Information Division, Washington DC, 451. ADS.

Chertok, I.M., Grechnev, V.V., Belov, A.V., Abunin, A.A.: 2013, Magnetic flux of EUV arcade and dimming regions as a relevant parameter for early diagnostics of solar eruptions – sources of non-recurrent geomagnetic storms and Forbush decreases. *Solar Phys.* **282**, 175. DOI. ADS.

Cliver, E.W., Kahler, S.W., Reames, D.V.: 2004, Coronal shocks and solar energetic proton events. *Astrophys. J.* **605**, 902. DOI. ADS.

Corchado Albelo, M.F., Kazachenko, M.D., Lynch, B.J.: 2024, Inferring fundamental properties of the flare current sheet using flare ribbons: oscillations in the reconnection flux rates. *Astrophys. J.* **965**, 16. DOI. ADS.

Dalla, S., de Nolfo, G.A., Bruno, A., Giacalone, J., Laitinen, T., Thomas, S., Battarbee, M., Marsh, M.S.: 2020, 3D propagation of relativistic solar protons through interplanetary space. *Astron. Astrophys.* **639**, A105. DOI. ADS.

Domingo, V., Fleck, B., Poland, A.I.: 1995, The SOHO mission: an overview. *Solar Phys.* **162**, 1. DOI. ADS.

Firoz, K.A., Zhang, Q.M., Gan, W.Q., Li, Y.P., Rodríguez-Pacheco, J., Moon, Y.-J., Kudela, K., Park, Y.-D., Dorman, L.I.: 2014, An interpretation of GLE71 concurrent CME-driven shock wave. *Astrophys. J. Suppl.* **213**, 24. DOI. ADS.

Firoz, K.A., Gan, W.Q., Li, Y.P., Rodríguez-Pacheco, J., Su, Y.: 2017, On the time evolution of brightness, volume and height of a coronal source in an M-class flare. *Astrophys. Space Sci.* **362**, 113. DOI. ADS.

Fletcher, L., Hudson, H.: 2001, The magnetic structure and generation of EUV flare ribbons. *Solar Phys.* **204**, 69. DOI. ADS.

Gopalswamy, N., Xie, H., Yashiro, S., Akiyama, S., Mäkelä, P., Usoskin, I.G.: 2012, Properties of ground level enhancement events and the associated solar eruptions during solar cycle 23. *Space Sci. Rev.* **171**, 23. DOI. ADS.

Gopalswamy, N., Xie, H., Mäkelä, P., Yashiro, S., Akiyama, S., Uddin, W., Srivastava, A.K., Joshi, N.C., Chandra, R., Manoharan, P.K., et al.: 2013a, Height of shock formation in the solar corona inferred from observations of type II radio bursts and coronal mass ejections. *Adv. Space Res.* **51**, 1981. DOI. ADS.

Gopalswamy, N., Xie, H., Akiyama, S., Yashiro, S., Usoskin, I.G., Davila, J.M.: 2013b, The first ground level enhancement event of solar cycle 24: direct observation of shock formation and particle release heights. *Astrophys. J. Lett.* **765**, L30. DOI. ADS.

Gopalswamy, N., Yashiro, S., Akiyama, S., Xie, H.: 2017, Estimation of reconnection flux using post-eruption arcades and its relevance to magnetic clouds at 1 AU. *Solar Phys.* **292**, 65. DOI. ADS.

Grechnev, V.V., Kiselev, V.I., Uralov, A.M.: 2022, Reconciling observational challenges to the impulsive-piston shock-excitation scenario. I. Kinematic challenges. *Solar Phys.* **297**, 106. DOI.

Grechnev, V.V., Kochanov, A.A., Uralov, A.M.: 2023, Eruptive flare, CME, and shock wave in the 25 August 2001 high-energy solar event. *Solar Phys.* **298**, 49. DOI. ADS.

Grechnev, V.V., Kuzmenko, I.V.: 2020, A geoeffective CME caused by the eruption of a quiescent prominence on 29 September 2013. *Solar Phys.* **295**, 55. DOI. ADS.

Grechnev, V.V., Uralov, A.M., Slemzin, V.A., Chertok, I.M., Kuzmenko, I.V., Shibasaki, K.: 2008, Absorption phenomena and a probable blast wave in the 13 July 2004 eruptive event. *Solar Phys.* **253**, 263. DOI. ADS.

Grechnev, V.V., Uralov, A.M., Chertok, I.M., Kuzmenko, I.V., Afanasyev, A.N., Meshalkina, N.S., Kalashnikov, S.S., Kubo, Y.: 2011, Coronal shock waves, EUV waves, and their relation to CMEs. I. Reconciliation of "EIT waves", type II radio bursts, and leading edges of CMEs. *Solar Phys.* **273**, 433. DOI. ADS.

Grechnev, V.V., Meshalkina, N.S., Chertok, I.M., Kiselev, V.I.: 2013, Relations between strong high-frequency microwave bursts and proton events. *Publ. Astron. Soc. Japan* **65**, S4. DOI. ADS.

Grechnev, V.V., Uralov, A.M., Slemzin, V.A., Chertok, I.M., Filippov, B.P., Rudenko, G.V., Temmer, M.: 2014a, A challenging solar eruptive event of 18 November 2003 and the causes of the 20 November geomagnetic superstorm. I. Unusual history of an eruptive filament. *Solar Phys.* **289**, 289. DOI. ADS.

Grechnev, V.V., Uralov, A.M., Chertok, I.M., Slemzin, V.A., Filippov, B.P., Egorov, Y.I., Fainshtein, V.G., Afanasyev, A.N., Prestage, N.P., Temmer, M.: 2014b, A challenging solar eruptive event of 18 November 2003 and the causes of the 20 November geomagnetic superstorm. II. CMEs, shock waves, and drifting radio bursts. *Solar Phys.* **289**, 1279. DOI. ADS.

Grechnev, V.V., Kiselev, V.I., Meshalkina, N.S., Chertok, I.M.: 2015, Relations between microwave bursts and near-Earth high-energy proton enhancements and their origin. *Solar Phys.* **290**, 2827. DOI. ADS.

Grechnev, V.V., Kiselev, V.I., Uralov, A.M., Klein, K.-L., Kochanov, A.A.: 2017, The 26 December 2001 solar eruptive event responsible for GLE63: III. CME, shock waves, and energetic particles. *Solar Phys.* **292**, 102. DOI. ADS.

Grechnev, V.V., Kochanov, A.A., Uralov, A.M., Slemzin, V.A., Rodkin, D.G., Goryaev, F.F., Kiselev, V.I., Myshyakov, I.I.: 2019, Development of a fast CME and properties of a related interplanetary transient. *Solar Phys.* **294**, 139. DOI. ADS.

Grechnev, V.V., Kiselev, V.I., Uralov, A.M., Myshyakov, I.I.: 2022, Reconciling observational challenges to the impulsive-piston shock-excitation scenario. II. Shock waves produced in CME-less events with a null-point topology. *Solar Phys.* **297**, 123. DOI. ADS.

Harvey, J.W.: 1969, Magnetic fields associated with solar active-region prominences. PhD thesis, National Solar Observatory, Sunspot New Mexico. ADS.

Hirayama, T.: 1974, Theoretical model of flares and prominences. I: Evaporating flare model. *Solar Phys.* **34**, 323. DOI. ADS.

Howard, R.A., Vourlidas, A., Stenborg, G.: 2023, The evolution of our understanding of coronal mass ejections. *Front. Astron. Space Sci.* **10**, 1264226. DOI. ADS.

Howard, R.A., Moses, J.D., Vourlidas, A., Newmark, J.S., Socker, D.G., Plunkett, S.P., Korendyke, C.M., Cook, J.W., Hurley, A., Davila, J.M., et al.: 2008, Sun Earth Connection Coronal and Heliospheric Investigation (SECCHI). *Space Sci. Rev.* **136**, 67. DOI. ADS.

Inhester, B., Birn, J., Hesse, M.: 1992, The evolution of line tied coronal arcades including a converging footpoint motion. *Solar Phys.* **138**, 257. DOI. ADS.

Kaiser, M.L., Kucera, T.A., Davila, J.M., St. Cyr, O.C., Guhathakurta, M., Christian, E.: 2008, The STEREO mission: an introduction. *Space Sci. Rev.* **136**, 5. DOI. ADS.

Kallenrode, M.-B.: 2003, Current views on impulsive and gradual solar energetic particle events. *J. Phys. G, Nucl. Part. Phys.* **29**, 965. ADS.

Kazachenko, M.D., Lynch, B.J., Welsch, B.T., Sun, X.: 2017, A database of flare ribbon properties from the Solar Dynamics Observatory. I. Reconnection flux. *Astrophys. J.* **845**, 49. DOI. ADS.

Khan, J.I., Bain, H.M., Fletcher, L.: 2007, The relative timing of supra-arcade downflows in solar flares. *Astron. Astrophys.* **475**, 333. DOI. ADS.

Klein, K.-L., Trottet, G.: 2001, The origin of solar energetic particle events: coronal acceleration versus shock wave acceleration. *Space Sci. Rev.* **95**, 215. ADS.

Knock, S.A., Cairns, I.H.: 2005, Type II radio emission predictions: sources of coronal and interplanetary spectral structure. *J. Geophys. Res.* **110**, A01101. DOI. ADS.

Kocharov, L., Pohjolainen, S., Mishev, A., Reiner, M.J., Lee, J., Laitinen, T., Didkovsky, L.V., Pizzo, V.J., Kim, R., Klassen, A., Karlicky, M., Cho, K.-S., Gary, D.E., Usoskin, I., Valtonen, E., Vainio, R.: 2017, Investigating the origins of two extreme solar particle events: proton source profile and associated electromagnetic emissions. *Astrophys. J.* **839**, 79. DOI. ADS.

Kopp, R.A., Pneuman, G.W.: 1976, Magnetic reconnection in the corona and the loop prominence phenomenon. *Solar Phys.* **50**, 85. DOI. ADS.

Lemen, J.R., Title, A.M., Akin, D.J., Boerner, P.F., Chou, C., Drake, J.F., Duncan, D.W., Edwards, C.G., Friedlaender, F.M., Heyman, G.F., et al.: 2012, The Atmospheric Imaging Assembly (AIA) on the Solar Dynamics Observatory (SDO). *Solar Phys.* **275**, 17. DOI. ADS.

Li, G., Moore, R., Mewaldt, R.A., Zhao, L., Labrador, A.W.: 2012, A twin-CME scenario for ground level enhancement events. *Space Sci. Rev.* **171**, 141. DOI. ADS.

Li, C., Firoz, K.A., Sun, L.P., Miroshnichenko, L.I.: 2013, Electron and proton acceleration during the first ground level enhancement event of solar cycle 24. *Astrophys. J.* **770**, 34. DOI. ADS.

Lin, J., Mancuso, S., Vourlidas, A.: 2006, Theoretical investigation of the onsets of type II radio bursts during solar eruptions. *Astrophys. J.* **649**, 1110. DOI. ADS.

Lin, R.P., Dennis, B.R., Hurford, G.J., Smith, D.M., Zehnder, A., Harvey, P.R., Curtis, D.W., Pankow, D., Turin, P., Bester, M., et al.: 2002, The Reuven Ramaty High-Energy Solar Spectroscopic Imager (RHESSI). *Solar Phys.* **210**, 3. DOI. ADS.

Linton, M.G., Longcope, D.W.: 2006, A model for patchy reconnection in three dimensions. *Astrophys. J.* **642**, 1177. DOI. ADS.

Longcope, D.W., Beveridge, C.: 2007, A quantitative, topological model of reconnection and flux rope formation in a two-ribbon flare. *Astrophys. J.* **669**, 621. DOI. ADS.

Masson, S., Antiochos, S.K., DeVore, C.R.: 2013, A model for the escape of solar-flare-accelerated particles. *Astrophys. J.* **771**, 82. DOI. ADS.

McKenzie, D.E.: 2000, Supra-arcade downflows in long-duration solar flare events. *Solar Phys.* **195**, 381. DOI. ADS.

McKenzie, D.E., Hudson, H.S.: 1999, X-ray observations of motions and structure above a solar flare arcade. *Astrophys. J. Lett.* **519**, L93. DOI. ADS.

Miklenic, C.H., Veronig, A.M., Vršnak, B.: 2009, Temporal comparison of nonthermal flare emission and magnetic-flux change rates. *Astron. Astrophys.* **499**, 893. DOI. ADS.

Miroshnichenko, L.I., Vashenyuk, E.V., Pérez-Peraza, J.A.: 2013, Solar cosmic rays: 70 years of ground-based observations. *Geomagn. Aeron.* **53**, 541. DOI. ADS.

Moraal, H., McCracken, K.G.: 2012, The time structure of ground level enhancements in solar cycle 23. *Space Sci. Rev.* **171**, 85. DOI. ADS.

Nitta, N.V., Schrijver, C.J., Title, A.M., Liu, W.: 2013, Large-scale coronal propagating fronts in solar eruptions as observed by the Atmospheric Imaging Assembly on board the Solar Dynamics Observatory—an ensemble study. *Astrophys. J.* **776**, 58. DOI. ADS.

Palmerio, E., Kilpua, E.K.J., Witasse, O., Barnes, D., Sánchez-Cano, B., Weiss, A.J., Nieves-Chinchilla, T., Möstl, C., Jian, L.K., Mierla, M., et al.: 2021, CME magnetic structure and IMF preconditioning affecting SEP transport. *Space Weather* **19**, e2020SW002654. DOI. ADS.

Pérez-Peraza, J., Márquez-Adame, J.C., Miroshnichenko, L., Velasco-Herrera, V.: 2018, Source energy spectrum of the 17 May 2012 GLE. *J. Geophys. Res. Space Phys.* **123**, 3262. DOI. ADS.

Pesnell, W.D., Thompson, B.J., Chamberlin, P.C.: 2012, The Solar Dynamics Observatory (SDO). *Solar Phys.* **275**, 3. DOI. ADS.

Prestage, N.P., Luckhurst, R.G., Paterson, B.R., Bevins, C.S., Yuile, C.G.: 1994, A new radio spectrograph at Culgoora. *Solar Phys.* **150**, 393. DOI. ADS.

Qiu, J., Wang, H., Cheng, C.Z., Gary, D.E.: 2004, Magnetic reconnection and mass acceleration in flare-coronal mass ejection events. *Astrophys. J.* **604**, 900. DOI. ADS.

Qiu, J., Hu, Q., Howard, T.A., Yurchyshyn, V.B.: 2007, On the magnetic flux budget in low-corona magnetic reconnection and interplanetary coronal mass ejections. *Astrophys. J.* **659**, 758. DOI. ADS.

Reames, D.V.: 2009, Solar release times of energetic particles in ground-level events. *Astrophys. J.* **693**, 812. DOI. ADS.

Reames, D.V.: 2013, The two sources of solar energetic particles. *Space Sci. Rev.* **175**, 53. DOI. ADS.

Rouillard, A.P., Plotnikov, I., Pinto, R.F., Tirole, M., Lavarra, M., Zucca, P., Vainio, R., Tylka, A.J., Vourlidas, A., De Rosa, M.L., Linker, J., Warmuth, A., Mann, G., Cohen, C.M.S., Mewaldt, R.A.: 2016, Deriving the properties of coronal pressure fronts in 3D: application to the 2012 May 17 ground level enhancement. *Astrophys. J.* **833**, 45. DOI. ADS.

Santandrea, S., Gantois, K., Strauch, K., Teston, F., Proba2 Project Team, Tilmans, E., Baijot, C., Gerrits, D., Proba2 Industry Team, de Groof, A., Schwehm, G., Zender, J.: 2013, PROBA2: mission and spacecraft overview. *Solar Phys.* **286**, 5. DOI. ADS.

Scherrer, P.H., Schou, J., Bush, R.I., Kosovichev, A.G., Bogart, R.S., Hoeksema, J.T., Liu, Y., Duvall, T.L., Zhao, J., Title, A.M., et al.: 2012, The Helioseismic and Magnetic Imager (HMI) investigation for the Solar Dynamics Observatory (SDO). *Solar Phys.* **275**, 207. DOI. ADS.

Shanmugaraju, A., Moon, Y.-J., Vrsnak, B.: 2009, Type II radio bursts with high and low starting frequencies. *Solar Phys.* **254**, 297. DOI. ADS.

Sheeley, N.R., Hakala, W.N., Wang, Y.-M.: 2000, Detection of coronal mass ejection associated shock waves in the outer corona. *J. Geophys. Res.* **105**, 5081. DOI. ADS.

Shen, C., Li, G., Kong, X., Hu, J., Sun, X.D., Ding, L., Chen, Y., Wang, Y., Xia, L.: 2013, Compound twin coronal mass ejections in the 2012 May 17 GLE event. *Astrophys. J.* **763**, 114. DOI. ADS.

Sturrock, P.A.: 1966, Model of the high-energy phase of solar flares. *Nature* **211**, 695. DOI. ADS.

Sun, X.: 2013, On the coordinate system of space-weather HMI Active Region Patches (SHARPs): a technical note. ArXiv e-prints. arXiv. ADS.

Temmer, M., Veronig, A.M., Vršnak, B., Rybák, J., Gömöry, P., Stoiser, S., Maričić, D.: 2008, Acceleration in fast halo CMEs and synchronized flare HXR bursts. *Astrophys. J. Lett.* **673**, L95. DOI. ADS.

Temmer, M., Vršnak, B., Žic, T., Veronig, A.M.: 2009, Analytic modeling of the Moreton wave kinematics. *Astrophys. J.* **702**, 1343. DOI. ADS.

Temmer, M., Veronig, A.M., Kontar, E.P., Krucker, S., Vršnak, B.: 2010, Combined STEREO/RHESSI study of coronal mass ejection acceleration and particle acceleration in solar flares. *Astrophys. J.* **712**, 1410. DOI. ADS.

Thernisien, A.: 2011, Implementation of the Graduated Cylindrical Shell model for the three-dimensional reconstruction of coronal mass ejections. *Astrophys. J. Suppl.* **194**, 33. DOI. ADS.

Thernisien, A., Vourlidas, A., Howard, R.A.: 2009, Forward modeling of coronal mass ejections using STEREO/SECCHI data. *Solar Phys.* **256**, 111. DOI. ADS.

Tschernitz, J., Veronig, A.M., Thalmann, J.K., Hinterreiter, J., Pötzi, W.: 2018, Reconnection fluxes in eruptive and confined flares and implications for superflares on the Sun. *Astrophys. J.* **853**, 41. DOI. ADS.

Umuhire, A.C., Gopalswamy, N., Uwamahoro, J., Akiyama, S., Yashiro, S., Mäkelä, P.: 2021, Properties of high-frequency type II radio bursts and their relation to the associated coronal mass ejections. *Solar Phys.* **296**, 27. DOI. ADS.

Uralov, A.M., Grechnev, V.V., Hudson, H.S.: 2005, Initial localization and kinematic characteristics of the structural components of a coronal mass ejection. *J. Geophys. Res. Space Phys.* **110**, A05104. DOI. ADS.

Uralov, A.M., Grechnev, V.V., Ivanukin, L.A.: 2019, Self-similar piston-shock and CME. *Solar Phys.* **294**, 113. DOI. ADS.

Uralova, S.V., Uralov, A.M.: 1994, WKB approach to the problem of magnetohydrodynamic shock propagation through the heliospheric current sheet. *Solar Phys.* **152**, 457. DOI. ADS.

Vourlidas, A., Wu, S.T., Wang, A.H., Subramanian, P., Howard, R.A.: 2003, Direct detection of a coronal mass ejection-associated shock in Large Angle and Spectrometric Coronagraph experiment white-light images. *Astrophys. J.* **598**, 1392. DOI. ADS.

Vourlidas, A., Lynch, B.J., Howard, R.A., Li, Y.: 2013, How many CMEs have flux ropes? Deciphering the signatures of shocks, flux ropes, and prominences in coronagraph observations of CMEs. *Solar Phys.* **284**, 179. DOI. ADS.

Vršnak, B.: 2016, Solar eruptions: the CME-flare relationship. *Astron. Nachr.* **337**, 1002. DOI. ADS.

Vršnak, B., Cliver, E.W.: 2008, Origin of coronal shock waves. Invited review. *Solar Phys.* **253**, 215. DOI. ADS.

Vršnak, B., Žic, T., Lulić, S., Temmer, M., Veronig, A.M.: 2016, Formation of coronal large-amplitude waves and the chromospheric response. *Solar Phys.* **291**, 89. DOI. ADS.

Warmuth, A., Vršnak, B., Aurass, H., Hanslmeier, A.: 2001, Evolution of two EIT/Hα Moreton waves. *Astrophys. J. Lett.* **560**, L105. DOI. ADS.

Warmuth, A., Vršnak, B., Magdalenić, J., Hanslmeier, A., Otruba, W.: 2004, A multiwavelength study of solar flare waves. I. Observations and basic properties. *Astron. Astrophys.* **418**, 1101. DOI. ADS.

Whitman, K., Bindi, V., Consolandi, C., Corti, C., Yamashiro, B.: 2017, Implications of improved measurements of the highest energy SEPs by AMS and PAMELA. *Adv. Space Res.* **60**, 768. DOI. ADS.

Wuelser, J.-P., Lemen, J.R., Tarbell, T.D., Wolfson, C.J., Cannon, J.C., Carpenter, B.A., Duncan, D.W., Gradwohl, G.S., Meyer, S.B., Moore, A.S., et al.: 2004, EUVI: the STEREO-SECCHI extreme ultraviolet imager. In: Fineschi, S., Gummin, M.A. (eds.) *Telescopes and Instrumentation for Solar Astrophysics*, *Society of Photo-Optical Instrumentation Engineers (SPIE) Conference Series* **5171**, 111. DOI. ADS.

Yashiro, S., Gopalswamy, N., Michalek, G., St. Cyr, O.C., Plunkett, S.P., Rich, N.B., Howard, R.A.: 2004, A catalog of white light coronal mass ejections observed by the SOHO spacecraft. *J. Geophys. Res. Space Phys.* **109**, A07105. DOI. ADS.

Zhang, J., Dere, K.P., Howard, R.A., Kundu, M.R., White, S.M.: 2001, On the temporal relationship between coronal mass ejections and flares. *Astrophys. J.* **559**, 452. DOI. ADS.

Zimovets, I., Vilmer, N., Chian, A.C.-L., Sharykin, I., Struminsky, A.: 2012, Spatially resolved observations of a split-band coronal type II radio burst. *Astron. Astrophys.* **547**, A6. DOI. ADS.